

Mechanical Models of Pattern and Form in Biological Tissues: The Role of Stress–Strain Constitutive Equations

Original

Mechanical Models of Pattern and Form in Biological Tissues: The Role of Stress–Strain Constitutive Equations / Villa, C.; Chaplain, M. A. J.; Gerisch, A.; Lorenzi, T.. - In: BULLETIN OF MATHEMATICAL BIOLOGY. - ISSN 0092-8240. - 83:7(2021), p. 80. [10.1007/s11538-021-00912-5]

Availability:

This version is available at: 11583/2920758 since: 2021-09-03T08:04:55Z

Publisher:

Springer

Published

DOI:10.1007/s11538-021-00912-5

Terms of use:

This article is made available under terms and conditions as specified in the corresponding bibliographic description in the repository

Publisher copyright

(Article begins on next page)



Mechanical Models of Pattern and Form in Biological Tissues: The Role of Stress–Strain Constitutive Equations

Chiara Villa¹  · Mark A. J. Chaplain¹  · Alf Gerisch²  · Tommaso Lorenzi³ 

Received: 23 September 2020 / Accepted: 11 May 2021
© The Author(s) 2021, corrected publication 2021

Abstract

Mechanical and mechanochemical models of pattern formation in biological tissues have been used to study a variety of biomedical systems, particularly in developmental biology, and describe the physical interactions between cells and their local surroundings. These models in their original form consist of a balance equation for the cell density, a balance equation for the density of the extracellular matrix (ECM), and a force–balance equation describing the mechanical equilibrium of the cell–ECM system. Under the assumption that the cell–ECM system can be regarded as an isotropic linear viscoelastic material, the force–balance equation is often defined using the Kelvin–Voigt model of linear viscoelasticity to represent the stress–strain relation of the ECM. However, due to the multifaceted bio-physical nature of the ECM constituents, there are rheological aspects that cannot be effectively captured by this model and, therefore, depending on the pattern formation process and the type of biological tissue considered, other constitutive models of linear viscoelasticity may be better suited. In this paper, we systematically assess the pattern formation potential of different stress–strain constitutive equations for the ECM within a mechanical model of pattern formation in biological tissues. The results obtained through linear stability analysis and the dispersion relations derived therefrom support the idea that fluid-like con-

✉ Mark A. J. Chaplain
majc@st-andrews.ac.uk

Chiara Villa
cv23@st-andrews.ac.uk

Alf Gerisch
gerisch@mathematik.tu-darmstadt.de

Tommaso Lorenzi
tommaso.lorenzi@polito.it

- ¹ School of Mathematics and Statistics, University of St Andrews, St Andrews 16 9SS, UK
- ² Fachbereich Mathematik, Technische Universität Darmstadt, Dolivostr. 15, 64293 Darmstadt, Germany
- ³ Department of Mathematical Sciences “G. L. Lagrange”, Dipartimento di Eccellenza 2018–2022, Politecnico di Torino, 10129 Torino, Italy

stitutive models, such as the Maxwell model and the Jeffrey model, have a pattern formation potential much higher than solid-like models, such as the Kelvin–Voigt model and the standard linear solid model. This is confirmed by the results of numerical simulations, which demonstrate that, all else being equal, spatial patterns emerge in the case where the Maxwell model is used to represent the stress–strain relation of the ECM, while no patterns are observed when the Kelvin–Voigt model is employed. Our findings suggest that further empirical work is required to acquire detailed quantitative information on the mechanical properties of components of the ECM in different biological tissues in order to furnish mechanical and mechanochemical models of pattern formation with stress–strain constitutive equations for the ECM that provide a more faithful representation of the underlying tissue rheology.

Keywords Pattern formation · Mechanical models · Murray–Oster theory · Biological tissues · Stress–strain constitutive equations · Linear viscoelasticity

1 Introduction

Pattern formation resulting from spatial organisation of cells is at the basis of a broad spectrum of physiological and pathological processes in living tissues (Jernvall et al. 2003). While the first formal exploration of pattern and form from a mathematical (strictly speaking, geometrical) perspective goes back over a century to D’Arcy Thompson’s “*On Growth and Form*” (Thompson 1917), the modern development of mathematical models for this biological phenomenon started halfway through the twentieth century to elucidate the mechanisms that underly morphogenesis and embryogenesis (Maini 2005). Since then, a number of mathematical models for the formation of cellular patterns have been developed (Urdu 2012). Amongst these, particular attention has been given to reaction–diffusion models and mechanochemical models of pattern formation (Murray 2001).

Reaction–diffusion models of pattern formation, first proposed by Turing in his seminal 1952 paper (Turing 1952) and then further developed by Gierer and Meinhardt (Gierer and Meinhardt 1972; Meinhardt 1982), apply to scenarios in which the heterogeneous spatial distribution of some chemicals (i.e. morphogens) acts as a template (i.e. a pre-pattern) according to which cells organise and arrange themselves in different sorts of spatial patterns. These models are formulated as coupled systems of reaction–diffusion equations for the space-time dynamics of the concentrations of two morphogens, with different reaction kinetics depending on the biological problem at stake. Such systems exhibit diffusion-driven instability whereby homogenous steady states are driven unstable by diffusion, resulting in the formation of pre-patterns, provided that the diffusion rate of one of the morphogens is sufficiently higher than the other (Maini et al. 1997; Maini and Woolley 2019; Maini et al. 2012; Murray 1981).

On the other hand, mechanochemical models of pattern formation, first proposed by Murray, Oster and coauthors in the 1980s (Murray and Oster 1984a, b; Murray et al. 1983; Oster et al. 1983), describe spatial organisation of cells driven by the mechanochemical interaction between cells and the extracellular matrix (ECM)—i.e. the substratum composed of collagen fibres and various macromolecules, partly pro-

duced by the cells themselves, in which cells are embedded (Harris 1984; Harris et al. 1981). These models in their original form consist of systems of partial differential equations (PDEs) comprising a balance equation for the cell density, a balance equation for the ECM density, and a force-balance equation describing the mechanical equilibrium of the cell-ECM system (Murray and Maini 1989; Murray et al. 1988). When chemical processes are neglected, these models reduce to mechanical models of pattern formation (Byrne and Chaplain 1996; Murray and Maini 1989; Murray et al. 1988).

While reaction–diffusion models well explain the emergence and characteristics of patterns arising during chemical reactions (Castets et al. 1990; Maini et al. 1997; Maini and Woolley 2019), as well as pigmentation patterns found on shells (Meinhardt 2009) or animal coatings (Kondo and Asai 1995; Murray 2001), various observations seem to suggest they may not always be the most suited models to study morphogenic pattern formation (Bard and Lauder 1974; Brinkmann et al. 2018; Maini and Woolley 2019). For instance, experiments up to this day seem to fail in the identification of appropriate morphogens and overall molecular interactions predicted by Turing models in order for *de novo* patterns to emerge may be too complex. In addition, unrealistic parameter values would be required in order to reproduce experimentally observable patterns and the models appear to be too sensitive to parameter changes, hence lacking the robustness required to capture precise patterns. These considerations indicate that other mechanisms, driven for instance by significant mechanical forces, should be considered since solely chemical interactions may not suffice in explaining the emergence of patterns during morphogenesis. Hence, mechanochemical models may be better suited. Interestingly, this need to change modelling framework sometimes arises within the same biological application as time progresses. For instance, supra-cellular organisation in the early stages of embryonic development closely follows morphogenic chemical patterns, but further tissue-level organisation requires additional cooperation of osmotic pressures and mechanical forces (Petrolli et al. 2019). Similarly, pattern formation during vasculogenesis is generally divided into an early stage highly driven by cell migration following chemical cues, and a later one dominated by mechanical interactions between the cells and the ECM (Ambrosi et al. 2005; Scianna et al. 2013; Tosin et al. 2006). Finally, purely mechanical models are a useful tool for studying the isolated role of mechanical forces and can capture observed phenomena without the inclusion of chemical cues (Petrolli et al. 2019; Serra-Picamal et al. 2012; Tlili et al. 2018).

Over the years, mechanochemical and mechanical models of pattern formation in biological tissues have been used to study a variety of biomedical problems, including morphogenesis and embryogenesis (Brinkmann et al. 2018; Cruywagen and Murray 1992; Maini and Murray 1988; Murray and Maini 1986; Murray et al. 1988; Murray and Oster 1984a, b; Murray et al. 1983; Oster et al. 1983; Perelson et al. 1986), angiogenesis and vasculogenesis (Manoussaki 2003; Scianna et al. 2013; Tranqui and Tracqui 2000), cytoskeleton reorganisation (Alonso et al. 2017; Lewis and Murray 1991), wound healing and contraction (Javierre et al. 2009; Maini et al. 2002; Olsen et al. 1995; Tranquillo and Murray 1992), and stretch marks (Gilmore et al. 2012). These models have also been used to estimate the values of cell mechanical parameters, with a particular focus on cell traction forces (Barocas et al. 1995; Barocas and

Tranquillo 1994; Benti and Murray 1991; Ferrenq et al. 1997; Moon and Tranquillo 1993; Perelson et al. 1986). The roles that different biological processes play in the formation of cellular patterns can be disentangled via linear stability analysis (LSA) of the homogenous steady states of the model equations—i.e. investigating what parameters of the model, and thus what biological processes, can drive homogenous steady states unstable and promote the emergence of cell spatial organisation. Further insight into certain aspects of pattern formation in biological tissues can also be provided by nonlinear stability analysis of the homogenous steady states (Cruywagen and Murray 1992; Lewis and Murray 1991; Maini and Murray 1988).

These models usually rely on the assumption that the cell-ECM system can be regarded as an isotropic linear viscoelastic material. This is clearly a simplification due to the nonlinear viscoelasticity and anisotropy of soft tissues (Bischoff et al. 2004; Huang et al. 2005; Liu and Bilston 2000; Nasser et al. 2002; Snedeker et al. 2005; Valtorta and Mazza 2005; Verdier 2003), a simplification that various rheological tests conducted on biological tissues have nonetheless shown to be justified in the regime of small strains (Bilston et al. 1997; Liu and Bilston 2000; Nasser et al. 2002; Valtorta and Mazza 2005), which is the one usually of interest in the applications of such models. Under this assumption, the force-balance equation for the cell-ECM system is often defined using the Kelvin–Voigt model of linear viscoelasticity to represent the stress–strain relation of the ECM (Byrne and Chaplain 1996; Murray et al. 1988; Oster et al. 1983). However, due to the multifaceted bio-physical nature of the ECM constituents, there are rheological aspects that cannot be effectively captured by the Kelvin–Voigt model and, therefore, depending on the pattern formation process and the type of biological tissue considered, other constitutive models of linear viscoelasticity may be better suited (Barocas and Tranquillo 1994). In this regard, Byrne and Chaplain (1996) demonstrated that, *ceteris paribus*, using the Maxwell model of linear viscoelasticity to describe the stress–strain relation of the ECM in place of the Kelvin–Voigt model can lead to different dispersion relations with a higher pattern formation potential. This suggests that a more thorough investigation of the capability of different stress–strain constitutive equations of producing spatial patterns is required.

With this aim, here we complement and further develop the results presented in Byrne and Chaplain (1996) by systematically assessing the pattern formation potential of different stress–strain constitutive equations for the ECM within a mechanical model of pattern formation in biological tissues (Byrne and Chaplain 1996; Murray et al. 1988; Oster et al. 1983). Compared to the work of Byrne and Chaplain (1996), here we consider a wider range of constitutive models, we allow cell traction forces to be reduced by cell–cell contact inhibition, and undertake numerical simulations of the model equations showing the formation of cellular patterns both in one and in two spatial dimensions. A related study has been conducted by Alonso et al. (2017), who considered a mathematical model of pattern formation in the cell cytoplasm.

The paper is structured as follows. In Sect. 2, we recall the essentials of viscoelastic materials and provide a brief summary of the one-dimensional stress–strain constitutive equations that we examine. In Sect. 3, we describe the one-dimensional mechanical model of pattern formation in biological tissues that is used in our study, which follows closely the one considered in Byrne and Chaplain (1996); Murray et al. (1988); Oster et al. (1983). In Sect. 4, we carry out a linear stability analysis (LSA) of a biologically

relevant homogeneous steady state of the model equations, derive dispersion relations when different stress–strain constitutive equations for the ECM are used and investigate how the model parameters affect the dispersion relations obtained. In Sect. 5, we verify key results of LSA via numerical simulations of the model equations. In Sect. 6, we complement these findings with the results of numerical simulations of a two-dimensional version of the mechanical model of pattern formation considered in the previous sections. Section 7 concludes the paper and provides an overview of possible research perspectives.

2 Essentials of Viscoelastic Materials and Stress–Strain Constitutive Equations

In this section, we first recall the main properties of viscoelastic materials (see Sect. 2.1). Then, we briefly present the one-dimensional stress–strain constitutive equations that are considered in our study and summarise the main rheological properties of linear viscoelastic materials that they capture (see Sect. 2.2). Most of the contents of this section can be found in standard textbooks, such as Findley et al. (1976) [chapters 1 and 5] and Mase (1970), and are reported here for the sake of completeness. Specific considerations of and applications to living tissues can be found in Fung (1993).

2.1 Essentials of Viscoelastic Materials

As the name suggests, viscoelastic materials exhibit both viscous and elastic characteristics, and the interplay between them may result in a wide range of rheological properties that can be examined through creep and stress relaxation tests. During a creep test, a constant stress is first applied to a specimen of material and then removed, and the time dynamic of the correspondent strain is tracked. During a stress relaxation test, a constant strain is imposed on a specimen of material and the evolution in time of the induced stress is observed (Findley et al. 1976).

Here, we list the main properties of viscoelastic materials that may be observed during the first phase of a creep test (see properties 1a–1c), during the recovery phase, that is, when the constant stress is removed from the specimen (see properties 2a–2c), and during a stress relaxation test (see property 3).

- 1a *Instantaneous elasticity*. As soon as a stress is applied, an instantaneous corresponding strain is observed.
- 1b *Delayed elasticity*. While the instantaneous elastic response to a stress is a purely elastic behaviour, due to the viscous nature of the material a delayed elastic response may also be observed. In this case, under constant stress the strain slowly and continuously increases at decreasing rate.
- 1c *Viscous flow*. In some viscoelastic materials, under a constant stress, the strain continues to grow within the viscoelastic regime (i.e. before plastic deformation). In particular, viscous flow occurs when the strain increases linearly with time and stops growing at removal of the stress only.

- 2a *Instantaneous recovery*. When the stress is removed, an instantaneous recovery (i.e. an instantaneous strain decrease) is observed because of the elastic nature of the material.
- 2b *Delayed recovery*. Upon removal of the stress, a delayed recovery (i.e. a continuous decrease in the strain at decreasing rate) occurs.
- 2c *Permanent set*. While elastic strain is reversible, in viscoelastic materials a nonzero strain, known as “permanent set” or “residual strain”, may persist even when the stress is removed.
- 3 *Stress relaxation*. Under constant strain, gradual relaxation of the induced stress occurs. In some cases, this may even culminate in total stress relaxation (i.e. the stress decays to zero).

The subset of these properties exhibited by a viscoelastic material will depend on—and hence define—the type of material being tested. Moreover, during each phase of the creep test, more than one of the above properties may be observed. For instance, a Maxwell material under constant stress will exhibit instantaneous elasticity followed by viscous flow.

2.2 One-Dimensional Stress–Strain Constitutive Equations Examined in Our Study

In this section, we briefly describe the different constitutive equations that are used in our study to represent the stress–strain relation of the ECM. In general, these equations can be used to predict how a viscoelastic material will react to different loading conditions, in one spatial dimension, and rely on the assumption that viscous and elastic characteristics of the material can be modelled, respectively, via linear combinations of dashpots and springs, as illustrated in Fig. 1. Different stress–strain constitutive equations correspond to different arrangements of these elements and capture different subsets of the rheological properties summarised in the previous section (see Table 2). In the remainder of this section, we will denote the stress and the strain at position x and time t by $\sigma(t, x)$ and $\varepsilon(t, x)$, respectively.

Linear elastic model. When viscous characteristics are neglected, a linear viscoelastic material can be modelled as a purely elastic spring with elastic modulus (i.e. Young’s modulus) $E > 0$, as illustrated in Fig. 1a. In this case, the stress–strain constitutive equation is given by Hooke’s spring law for continuous media, that is,

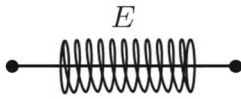
$$\sigma = E\varepsilon. \quad (1)$$

Linear viscous model. When elastic characteristics are neglected, a linear viscoelastic material can be modelled as a purely viscous damper of viscosity $\eta > 0$, as illustrated in Fig. 1b. In this case, the stress–strain constitutive equation is given by Newton’s law of viscosity, that is,

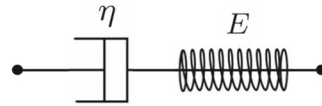
$$\sigma = \eta \partial_t \varepsilon. \quad (2)$$

Kelvin–Voigt model. The Kelvin–Voigt model, also known as the Voigt model, relies on the assumption that viscous and elastic characteristics of a linear viscoelastic material

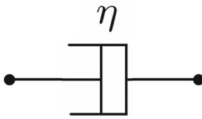
(a) Linear elastic model



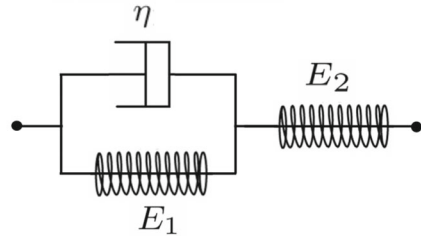
(d) Maxwell model



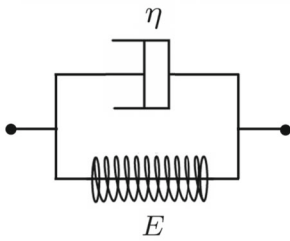
(b) Linear viscous model



(e) SLS model



(c) Kelvin-Voigt model



(f) Jeffrey model

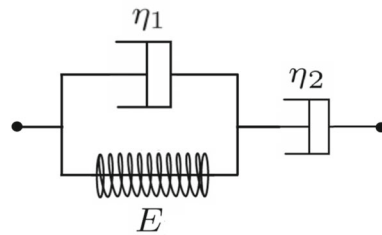


Fig. 1 Combinations of elastic springs and viscous dampers, together with the associated elastic (E, E_1, E_2) and viscous moduli (η, η_1, η_2), for the models of linear viscoelasticity considered in this work: the linear elastic model (a), the linear viscous model (b), the Kelvin–Voigt model (c), the Maxwell model (d), the SLS model (e), and the Jeffrey model (f)

can simultaneously be captured by considering a purely elastic spring with elastic modulus E and a purely viscous damper of viscosity η in parallel, as illustrated in Fig. 1c. The corresponding stress–strain constitutive equation is

$$\sigma = E\varepsilon + \eta \partial_t \varepsilon. \tag{3}$$

Maxwell model. The Maxwell model relies on the assumption that viscous and elastic characteristics of a linear viscoelastic material can be captured by considering a purely elastic spring with elastic modulus E and a purely viscous damper of viscosity η in series, as illustrated in Fig. 1d. The corresponding stress–strain constitutive equation is

$$\frac{1}{E} \partial_t \sigma + \frac{\sigma}{\eta} = \partial_t \varepsilon. \tag{4}$$

Standard linear solid (SLS) model. The SLS model, also known as the Kelvin model, relies on the assumption that viscous and elastic characteristics of a linear viscoelastic material can be captured by considering a Kelvin arm of elastic modulus E_1 and viscosity η in series with a purely elastic spring of elastic modulus E_2 , as illustrated in Fig. 1e. The corresponding stress–strain constitutive equation is [Mase \(1970\)](#)

$$\frac{1}{E_2} \partial_t \sigma + \frac{1}{\eta} \left(1 + \frac{E_1}{E_2} \right) \sigma = \partial_t \varepsilon + \frac{E_1}{\eta} \varepsilon. \tag{5}$$

Jeffrey model. The Jeffrey model, also known as the Oldroyd-B or 3-parameter viscous model, relies on the assumption that viscous and elastic characteristics of a linear viscoelastic material can be captured by considering a Kelvin arm of elastic modulus E and viscosity η_1 in series with a purely viscous damper of viscosity η_2 , as illustrated in Fig. 1f. The corresponding stress–strain constitutive equation is

$$\left(1 + \frac{\eta_1}{\eta_2} \right) \partial_t \sigma + \frac{E}{\eta_2} \sigma = \eta_1 \partial_{tt}^2 \varepsilon + E \partial_t \varepsilon. \tag{6}$$

Generic 4-parameter model. The following stress–strain constitutive equation encompasses all constitutive models of linear viscoelasticity whereby a combination of purely elastic springs and purely viscous dampers, up to a total of four elements, and therefore 4 parameters, is considered

$$a_2 \partial_{tt}^2 \sigma + a_1 \partial_t \sigma + a_0 \sigma = b_2 \partial_{tt}^2 \varepsilon + b_1 \partial_t \varepsilon + b_0 \varepsilon. \tag{7}$$

Here, the non-negative, real parameters $a_0, a_1, a_2, b_0, b_1, b_2$ depend on the elastic moduli and the viscosities of the underlying combinations of springs and dampers. When these parameters are defined as in [Table 1](#), the generic 4-parameter constitutive model (7) reduces to the specific stress–strain constitutive equations (1)–(6). For convenience of notation, we define the differential operators

$$\mathcal{L}_a := a_2 \partial_{tt}^2 + a_1 \partial_t + a_0 \quad \text{and} \quad \mathcal{L}_b := b_2 \partial_{tt}^2 + b_1 \partial_t + b_0 \tag{8}$$

so that the stress–strain constitutive equation (7) can be rewritten in the following compact form

$$\mathcal{L}_a[\sigma] = \mathcal{L}_b[\varepsilon]. \tag{9}$$

A summary of the rheological properties of linear viscoelastic materials listed in [Sect. 2.1](#) that are captured by the one-dimensional stress–strain constitutive Eqs. (1)–(6) is provided in [Table 2](#). These properties can be examined through mathematical procedures that mimic creep and stress relaxation tests ([Findley et al. 1976](#)). Notice that, for all these constitutive models, instantaneous elasticity correlates with instantaneous recovery, delayed elasticity correlates with delayed recovery, and viscous flow correlates with permanent set. Materials are said to be more solid-like when their elastic response dominates their viscous response, and more fluid-like in the opposite

Table 1 Relations between the generic 4-parameter model (7) and the stress–strain constitutive Eqs. (1)–(6)

Generic 4-parameters model	a_2	a_1	a_0	b_2	b_1	b_0
Linear elastic model	0	0	1	0	0	E
Linear viscous model	0	0	1	0	η	0
Kelvin-Voigt model	0	0	1	0	η	E
Maxwell model	0	$\frac{1}{E}$	$\frac{1}{\eta}$	0	1	0
SLS model	0	$\frac{1}{E_2}$	$\frac{1}{\eta} \left(1 + \frac{E_1}{E_2} \right)$	0	1	$\frac{E_1}{\eta}$
Jeffrey model	0	$1 + \frac{\eta_1}{\eta_2}$	$\frac{E}{\eta_2}$	η_1	E	0

case (Nargess and Yanlan 2021). For this reason, models of linear viscoelasticity that capture viscous flow and, as a consequence, permanent set—such as the Maxwell model and the Jeffrey model—are classified as “fluid-like models”, while those which do not—such as the Kelvin–Voigt model and the SLS model—are classified as “solid-like models”. In the remainder of the paper, we are going to include the linear viscous model in the fluid-like class and the linear elastic model in the solid-like class, as they capture—or do not capture—the relevant properties, even if they are not models of viscoelasticity *per se*.

3 A One-Dimensional Mechanical Model of Pattern Formation

We consider a one-dimensional region of tissue and represent the normalised densities of cells and ECM at time $t \in [0, T]$ and position $x \in [\ell, L]$ by means of the non-negative functions $n(t, x)$ and $\rho(t, x)$, respectively. We let $u(t, x)$ model the displacement of a material point of the cell-ECM system originally at position x , which is induced by mechanical interactions between cells and the ECM—i.e. cells pull on the ECM in which they are embedded, thus inducing ECM compression and densification which in turn cause a passive form of cell repositioning (Van Helvert et al. 2018).

3.1 Dynamics of the Cells

Following Murray et al. (1988); Oster et al. (1983), we consider a scenario where cells change their position according to a combination of: (i) undirected, random movement, which we describe through Fick’s first law of diffusion with diffusivity (i.e. cell motility) $D > 0$; (ii) haptotaxis (i.e. cell movement up the density gradient of the ECM) with haptotactic sensitivity $\alpha > 0$; (iii) passive repositioning caused by mechanical interactions between cells and the ECM, which is modelled as an advection with velocity field $\partial_t u$. Moreover, we model variation of the normalised cell density caused by cell proliferation and death via logistic growth with intrinsic growth rate $r > 0$ and unitary local carrying capacity. Under these assumptions, we describe cell

Table 2 Properties of linear viscoelastic materials captured by the stress-strain constitutive Eqs. (1)–(6)

	Instantaneous elasticity	Delayed elasticity	Viscous flow	Instantaneous recovery	Delayed recovery	Permanent set	Stress relaxation
Linear elastic model	✓			✓			
Linear viscous model			✓			✓	N. A.
Kelvin-Voigt model		✓			✓		
Maxwell model	✓		✓	✓		✓	✓
SLS model	✓	✓		✓	✓		✓
Jeffrey model		✓	✓		✓	✓	✓

dynamics through the following balance equation for $n(t, x)$

$$\partial_t n = \partial_x [D \partial_x n - n (\alpha \partial_x \rho + \partial_t u)] + r n (1 - n) \tag{10}$$

subject to suitable initial and boundary conditions.

3.2 Dynamics of the ECM

As was done for the cell dynamics, in a similar manner we model compression and densification of the ECM induced by cell-ECM interactions as an advection with velocity field $\partial_t u$. Furthermore, as in Murray et al. (1988); Oster et al. (1983), we neglect secretion of ECM components by the cells since this process occurs on a slower time scale compared to mechanical interactions between cells and the ECM. Under these assumptions, we describe the cell dynamics through the following transport equation for $\rho(t, x)$

$$\partial_t \rho = -\partial_x (\rho \partial_t u) \tag{11}$$

subject to suitable initial and boundary conditions.

3.3 Force-Balance Equation for the Cell-ECM System

Following Murray et al. (1988); Oster et al. (1983), we represent the cell-ECM system as a linear viscoelastic material with low Reynolds number (i.e. inertial terms are negligible compared to viscous terms) and we assume the cell-ECM system to be in mechanical equilibrium (i.e. traction forces generated by the cells are in mechanical equilibrium with viscoelastic restoring forces developed in the ECM and any other external forces). Under these assumptions, the force-balance equation for the cell-ECM system is of the form

$$\partial_x (\sigma_c + \sigma_m) + \rho F = 0, \tag{12}$$

where $\sigma_m(t, x)$ is the contribution to the stress of the cell-ECM system coming from the ECM, $\sigma_c(t, x)$ is the contribution to the stress of the cell-ECM system coming from the cells, and $F(t, x)$ is the external force per unit matrix density, which comes from the surrounding tissue that constitutes the underlying substratum to which the ECM is attached.

The stress σ_c is related to cellular traction forces acting on the ECM and is defined as

$$\sigma_c := \tau f(n) n (\rho + \beta \partial_{xx}^2 \rho) \quad \text{with} \quad f(n) := \frac{1}{1 + \lambda n^2}. \tag{13}$$

Definition (13) relies on the assumption that the stress generated by cell traction on the ECM is proportional to the cell density n and—in the short range—the ECM density ρ , while the term $\beta \partial_{xx}^2 \rho$ accounts for long-range cell traction effects, with β being

the long-range traction proportionality constant. The factor of proportionality is given by a positive parameter, τ , which measures the average traction force generated by a cell, multiplied by a non-negative and monotonically decreasing function of the cell density, $f(n)$, which models the fact that the average traction force generated by a cell is reduced by cell-cell contact inhibition (Murray 2001). The parameter $\lambda \geq 0$ measures the level of cell traction force inhibition and assuming $\lambda = 0$ corresponds to neglecting the reduction in the cell traction forces caused by cellular crowding.

The stress σ_m is given by the stress–strain constitutive equation that is used for the ECM, which we choose to be the general constitutive model (9) with the strain $\varepsilon(t, x)$ being given by the gradient of the displacement $u(t, x)$, that is, $\varepsilon = \partial_x u$. Therefore, we define the stress–strain relation of the ECM via the following equation

$$\mathcal{L}_a[\sigma_m] = \mathcal{L}_b[\partial_x u], \tag{14}$$

where the differential operators \mathcal{L}_a and \mathcal{L}_b are defined according to (8).

Assuming the surrounding tissue to which the ECM is attached to be a linear elastic material (Murray 2001), the external body force F can be modelled as a restoring force proportional to the cell-ECM displacement, that is,

$$F := -s u. \tag{15}$$

Here, the parameter $s > 0$ represents the elastic modulus of the surrounding tissue.

In order to obtain a closed equation for the displacement $u(t, x)$, we apply the differential operator $\mathcal{L}_a[\cdot]$ to the force-balance Eq. (12) and then substitute (13)–(15) into the resulting equation. In so doing, we find

$$\begin{aligned} \mathcal{L}_a[\partial_x(\sigma_m + \sigma_c)] &= -\mathcal{L}_a[\rho F] \\ \Leftrightarrow \mathcal{L}_a[\partial_x \sigma_m] + \mathcal{L}_a[\partial_x \sigma_c] &= \mathcal{L}_a[s\rho u] \\ \Leftrightarrow \partial_x \mathcal{L}_a[\sigma_m] &= \mathcal{L}_a[s\rho u] - \mathcal{L}_a[\partial_x \sigma_c] \\ \Leftrightarrow \partial_x \mathcal{L}_b[\partial_x u] &= \mathcal{L}_a[s\rho u - \partial_x \sigma_c] \\ \Leftrightarrow \mathcal{L}_b[\partial_{xx}^2 u] &= \mathcal{L}_a[s\rho u - \partial_x \sigma_c], \end{aligned}$$

that is,

$$\mathcal{L}_b[\partial_{xx}^2 u] = \mathcal{L}_a \left[s\rho u - \partial_x \left(\frac{\tau n}{1 + \lambda n^2} (\rho + \beta \partial_{xx}^2 \rho) \right) \right]. \tag{16}$$

Finally, to close the system, Eq. (16) needs to be supplied with suitable initial and boundary conditions.

3.4 Boundary Conditions

We close our mechanical model of pattern formation defined by the system of PDEs (10), (11) and (16) with the following boundary conditions

$$\left\{ \begin{array}{l} n(t, \ell) = n(t, L), \quad \partial_x n(t, \ell) = \partial_x n(t, L), \\ \rho(t, \ell) = \rho(t, L), \quad \partial_{xx}^2 \rho(t, \ell) = \partial_{xx}^2 \rho(t, L), \\ u(t, \ell) = u(t, L), \quad \partial_x u(t, \ell) = \partial_x u(t, L), \end{array} \right. \quad \text{for all } t \in [0, T]. \quad (17)$$

Here, the conditions on the derivatives of n , ρ and u ensure that the fluxes in Eqs. (10) and (11), and the overall stress ($\sigma_m + \sigma_c$) in Eq. (16), are periodic on the boundary, *i.e.* they ensure that

$$\left\{ \begin{array}{l} [D \partial_x n - n (\alpha \partial_x \rho + \partial_t u)]_{x=\ell} = [D \partial_x n - n (\alpha \partial_x \rho + \partial_t u)]_{x=L}, \\ [n \partial_t u]_{x=\ell} = [n \partial_t u]_{x=L}, \\ \left[\tau \frac{n}{(1 + \lambda^2)} (\rho + \beta \partial_{xx}^2 \rho) + \sigma_m \right]_{x=\ell} = \left[\tau \frac{n}{(1 + \lambda^2)} (\rho + \beta \partial_{xx}^2 \rho) + \sigma_m \right]_{x=L}, \end{array} \right. \quad \text{for all } t \in [0, T],$$

with σ_m given as a function of $\partial_x u$ in Eq. (14), according to the selected constitutive model. The periodic boundary conditions (17) reproduce a biological scenario in which the spatial region considered is part of a larger area of tissue whereby similar dynamics of the cells and the ECM occur.

4 Linear Stability Analysis and Dispersion Relations

In this section, we carry out LSA of a biologically relevant homogeneous steady state of the system of PDEs (10), (11) and (16) (see Sect. 4.1) and we compare the dispersion relations obtained when the constitutive models (1)–(6) are alternatively used to represent the contribution to the overall stress coming from the ECM, in order to explore the pattern formation potential of these stress–strain constitutive equations (see Sect. 4.2).

4.1 Linear Stability Analysis

Biologically relevant homogeneous steady state. All non-trivial homogeneous steady states $(\bar{n}, \bar{\rho}, \bar{u})^T$ of the system of PDEs (10), (11) and (16) subject to boundary conditions (17) have components $\bar{n} \equiv 1$ and $\bar{u} \equiv 0$, and we consider the arbitrary non-trivial steady state $\bar{\rho} \equiv \rho_0 > 0$ amongst the infinite number of possible homogeneous steady states of the transport Eq. (11) for the normalised ECM density ρ . Hence, we focus our attention on the biologically relevant homogeneous steady state $\bar{\mathbf{v}} = (1, \rho_0, 0)^T$. *Linear stability analysis to spatially homogeneous perturbations.* In order to undertake linear stability analysis of the steady state $\bar{\mathbf{v}} = (1, \rho_0, 0)^T$ to spatially homogeneous perturbations, we make the ansatz $\mathbf{v}(t, x) \equiv \bar{\mathbf{v}} + \tilde{\mathbf{v}}(t)$, where the vector $\tilde{\mathbf{v}}(t) = (\tilde{n}(t), \tilde{\rho}(t), \tilde{u}(t))^T$ models small spatially homogeneous perturbations and linearise the system of PDEs (10), (11) and (16) about the steady state $\bar{\mathbf{v}}$. Assuming

$\tilde{n}(t)$, $\tilde{\rho}(t)$ and $\tilde{u}(t)$ to be proportional to $\exp(\psi t)$, with $\psi \neq 0$, one can easily verify that ψ satisfies the algebraic equation $\psi(\psi + r)(\psi^2 a_2 + \psi a_1 + a_0) = 0$. Since r is positive and the parameters a_0, a_1 and a_2 are all non-negative, the solution ψ of such an algebraic equation is necessarily negative and, therefore, the small perturbations $\tilde{n}(t)$, $\tilde{\rho}(t)$ and $\tilde{u}(t)$ will decay to zero as $t \rightarrow \infty$. This implies that the steady state $\bar{\mathbf{v}}$ will be stable to spatially homogeneous perturbations for any choice of the parameter a_0, a_1, a_2, b_0, b_1 and b_2 in the stress–strain constitutive equation (14) (i.e. for all constitutive models (1)–(6)).

Linear stability analysis to spatially inhomogeneous perturbations. In order to undertake linear stability analysis of the steady state $\bar{\mathbf{v}} = (1, \rho_0, 0)^T$ to spatially inhomogeneous perturbations, we make the ansatz $\mathbf{v}(t, x) = \bar{\mathbf{v}} + \tilde{\mathbf{v}}(t, x)$, where the vector $\tilde{\mathbf{v}}(t, x) = (\tilde{n}(t, x), \tilde{\rho}(t, x), \tilde{u}(t, x))^T$ models small spatially inhomogeneous perturbations and linearise the system of PDEs (10), (11) and (16) about the steady state $\bar{\mathbf{v}}$. Assuming $\tilde{n}(t, x)$, $\tilde{\rho}(t, x)$ and $\tilde{u}(t, x)$ to be proportional to $\exp(\psi t + ikx)$, with $\psi \neq 0$ and $k \neq 0$, we find that ψ satisfies the following equation

$$\psi \left[c_3(k^2)\psi^3 + c_2(k^2)\psi^2 + c_1(k^2)\psi + c_0(k^2) \right] = 0, \tag{18}$$

with

$$c_3(k^2) := a_2\tau\lambda_1\beta k^4 + [b_2 - a_2\tau(\lambda_1 + \lambda_2\rho_0)]k^2 + a_2s\rho_0 \tag{19}$$

$$c_2(k^2) := a_2\tau\lambda_1 D\beta k^6 + [b_2D - a_2\tau(\lambda_2\rho_0\alpha + D\lambda_1 - r\lambda_1\beta) + a_1\tau\lambda_1\beta]k^4 + [b_2r + b_1 + a_2(Ds\rho_0 - r\tau\lambda_1) - a_1\tau(\lambda_1 + \lambda_2\rho_0)]k^2 + (a_1 + a_2r)s\rho_0 \tag{20}$$

$$c_1(k^2) := a_1\tau\lambda_1 D\beta k^6 + [b_1D - a_1\tau(\lambda_2\rho_0\alpha + D\lambda_1 - r\lambda_1\beta) + a_0\tau\lambda_1\beta]k^4 + [b_1r + b_0 + a_1(Ds\rho_0 - r\tau\lambda_1) - a_0\tau(\lambda_1 + \lambda_2\rho_0)]k^2 + (a_0 + a_1r)s\rho_0 \tag{21}$$

and

$$c_0(k^2) := a_0\tau\lambda_1 D\beta k^6 + [b_0D - a_0\tau(\lambda_2\rho_0\alpha + D\lambda_1 - r\lambda_1\beta)]k^4 + [b_0r + a_0(Ds\rho_0 - r\tau\lambda_1)]k^2 + a_0rs\rho_0 \tag{22}$$

where

$$\lambda_1 := \frac{1}{1 + \lambda} \quad \text{and} \quad \lambda_2 := \frac{(1 - \lambda)}{(1 + \lambda)^2}.$$

Equation (18) has multiple solutions $(\psi(k^2))$ for each k^2 , and we denote by $\text{Re}(\cdot)$ the maximum real part of all these solutions. For cell patterns to emerge, we need the non-trivial homogeneous steady state $\bar{\mathbf{v}}$ to be unstable to spatially inhomogeneous perturbations, that is, we need $\text{Re}(\psi(k^2)) > 0$ for some $k^2 > 0$. Notice that a necessary condition for this to happen is that at least one amongst $c_0(k^2), c_1(k^2), c_2(k^2)$ and $c_3(k^2)$ is negative for some $k^2 > 0$. Hence, the fact that if $\tau = 0$, then $c_0(k^2), c_1(k^2), c_2(k^2)$ and $c_3(k^2)$ are all non-negative for any value of k^2 allows us to conclude that

having $\tau > 0$ is a necessary condition for pattern formation to occur. This was expected based on the results presented in Murray (2001) and references therein.

In the case, where the model parameters are such that $c_2(k^2) = 0$ and $c_3(k^2) = 0$, solving Eq. (18) for ψ gives the following dispersion relation

$$\psi(k^2) = -\frac{c_0(k^2)}{c_1(k^2)} \tag{23}$$

and for the condition $\text{Re}(\psi(k^2)) > 0$ to be met it suffices that, for some $k^2 > 0$,

$$c_0(k^2) > 0 \text{ and } c_1(k^2) < 0 \text{ or } c_0(k^2) < 0 \text{ and } c_1(k^2) > 0.$$

On the other hand, when the model parameters are such that only $c_3(k^2) = 0$, from Eq. (18) we obtain the following dispersion relation

$$\psi(k^2) = \frac{-c_1(k^2) \pm \sqrt{(c_1(k^2))^2 - 4c_2(k^2)c_0(k^2)}}{2c_2(k^2)}, \tag{24}$$

and for the condition $\text{Re}(\psi(k^2)) > 0$ to be satisfied it is sufficient that one of the following four sets of conditions holds

$$c_2(k^2) > 0 \text{ and } c_0(k^2) < 0 \text{ or } c_2(k^2) > 0, \quad c_1(k^2) < 0 \text{ and } c_0(k^2) > 0$$

or

$$c_2(k^2) < 0 \text{ and } c_0(k^2) > 0 \text{ or } c_2(k^2) < 0, \quad c_1(k^2) > 0 \text{ and } c_0(k^2) < 0.$$

Finally, in the general case where the model parameters are such that $c_3(k^2) \neq 0$ as well, from Eq. (18) we obtain the following dispersion relation

$$\psi(k^2) = \left\{ q + \left[q^2 + (m - p^2)^3 \right]^{1/2} \right\}^{1/3} + \left\{ q - \left[q^2 + (m - p^2)^3 \right]^{1/2} \right\}^{1/3} + p, \tag{25}$$

where $p \equiv p(k^2)$, $q \equiv q(k^2)$ and $m \equiv m(k^2)$ are defined as

$$p := -\frac{c_2}{3c_3}, \quad q := p^3 + \frac{c_2c_1 - 3c_3c_0}{6c_3^2}, \quad m := \frac{c_1}{3c_3}.$$

In this case, identifying sufficient conditions to ensure that the real part of $\psi(k^2)$ is positive for some $k^2 > 0$ requires lengthy algebraic calculations. We refer the interested reader to Gilmore et al. (2012), where the Routh–Hurwitz stability criterion was used to analyse this general case and obtain more explicit conditions on the model parameters under which pattern formation occurs.

4.2 Dispersion Relations

Substituting the definitions of a_0, a_1, a_2, b_0, b_1 and b_2 corresponding to the stress–strain constitutive equations (1)–(6), which are reported in Table 1, into definitions (19)–(22) for $c_0(k^2), c_1(k^2), c_2(k^2)$ and $c_3(k^2)$, and then using the dispersion relation given by formula (23), (24) or (25) depending on the values of $c_2(k^2)$ and $c_3(k^2)$ so obtained, we derive the dispersion relation for each of the constitutive models (1)–(6). In particular, we are interested in whether the real part of each dispersion relation is positive, so whenever multiple roots are calculated—for instance using (24)—the largest root is considered. In addition, dispersion relations throughout this section are plotted against the quantity k/π , which directly correlates with perturbation modes and can therefore better highlight mode selection during the sensitivity analysis.

Base-case dispersion relations. Figure 2 displays the dispersion relations obtained for the stress–strain constitutive equations (1)–(6) under the following base-case parameter values

$$E = 1, \quad E_1 = E_2 = \frac{1}{2}E = 0.5, \quad \eta = 1, \quad \eta_1 = \eta_2 = \frac{1}{2}\eta = 0.5, \quad D = 0.01, \quad (26)$$

$$\rho_0 = 1, \quad \alpha = 0.05, \quad r = 1, \quad s = 10, \quad \lambda = 0.5, \quad \tau = 0.2 \quad \beta = 0.005. \quad (27)$$

The parameter values given by (26) and (27) are chosen for illustrative purposes, in order to highlight the different qualitative behaviour of the dispersion relations obtained using different models and are comparable with nondimensional parameter values that can be found in the extant literature (see Appendix A for further details). A comparison between the plots in Fig. 2 reveals that fluid-like models, that is, the linear viscous model (2), the Maxwell model (4), and the Jeffrey model (6) (*cf.* Table 2), have a higher pattern formation potential than solid-like models, since under the same parameter set they exhibit a range—or, more precisely, they exhibit the same range—of unstable modes (*i.e.* $\text{Re}(\psi(k^2)) > 0$ for a range of values of k/π), while the others have no unstable modes.

We now undertake a sensitivity analysis with respect to the different model parameters and discuss key changes that occur in the base-case dispersion relations displayed in Fig. 2.

ECM elasticity. The plots in Fig. 3 illustrate how the base-case dispersion relations displayed in Fig. 2 change when different values of the parameter E , and therefore also E_1 and E_2 (*i.e.* the parameters modelling ECM elasticity), are considered. These plots show that lower values of these parameters correlate with overall larger values of $\text{Re}(\psi(k^2))$ for all constitutive models, except for the linear viscous one, which corresponds to speeding up the formation of spatial patterns, when these may form. In addition, sufficiently small values of the parameters E, E_1 , and E_2 allow the linear elastic model (1), the Kelvin–Voigt model (3), and the SLS model (5) to exhibit unstable modes. However, further lowering the values of these parameters appears to lead to singular dispersion relations (*cf.* the plots for the linear elastic model (1), the Maxwell model (4), and the SLS model (5) in Fig. 3), which suggests that linear stability theory may fail in the regime of low ECM elasticity.

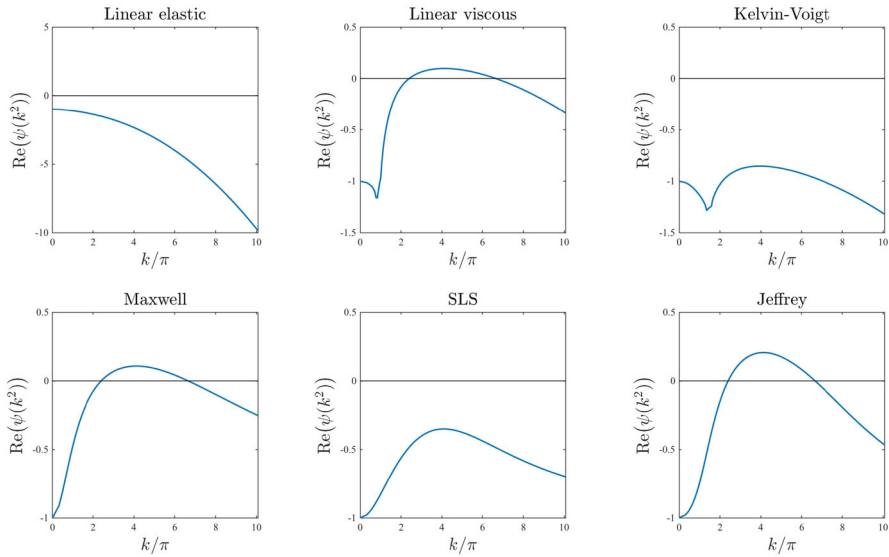


Fig. 2 Base-case dispersion relations. Dispersion relations corresponding to the stress–strain constitutive equations (1)–(6) for the base-case set of parameter values given by (26) and (27)

ECM viscosity. The plots in Fig. 4 illustrate how the base-case dispersion relations displayed in Fig. 2 change when different values of the parameter η , and therefore also η_1 and η_2 (i.e. the parameters modelling ECM viscosity), are considered. These plots show that larger values of these parameters leave the range of modes for which $\text{Re}(\psi(k^2)) > 0$ unchanged but reduce the values of $\text{Re}(\psi(k^2))$. This supports the idea that a higher ECM viscosity may not change the pattern formation potential of the different constitutive models but may slow down the corresponding pattern formation processes.

Cell motility. The plots in Fig. 5 illustrate how the base-case dispersion relations displayed in Fig. 2 change when different values of the parameter D (i.e. the parameter modelling cell motility) are considered. These plots show that larger values of this parameter may significantly shrink the range of modes for which $\text{Re}(\psi(k^2)) > 0$. In particular, with the exception of the linear elastic model, all constitutive models exhibit: infinitely many unstable modes when $D \rightarrow 0$; a finite number of unstable modes for intermediate values of D ; no unstable modes for sufficiently large values of D . This is to be expected due to the stabilising effect of undirected, random cell movement and indicates that higher cell motility may correspond to lower pattern formation potential.

Intrinsic growth rate of the cell density and elasticity of the surrounding tissue. The plots in Figs. 6 and 7 illustrate how the base-case dispersion relations displayed in Fig. 2 change when different values of the parameter r (i.e. the intrinsic growth rate of the cell density) and the parameter s (i.e. the elasticity of the surrounding tissue) are, respectively, considered. These plots show that considering larger values of these parameters reduces the values of $\text{Re}(\psi(k^2))$ for all constitutive models, and in par-

ticular it shrinks the range of unstable modes for the linear viscous model (2), the Maxwell model (4), and the Jeffrey model (6), which can become stable for values of r or s sufficiently large. This supports the idea that higher growth rates of the cell density (i.e. faster cell proliferation and death), and higher substrate elasticity (i.e. stronger external tethering force) may slow down pattern formation processes and overall reduce the pattern formation potential for all constitutive models. Moreover, the plots in Fig. 7 indicate that higher values of s may in particular reduce the pattern formation potential of the different constitutive models by making it more likely that $\text{Re}(\psi(k^2)) < 0$ for smaller values of k/π (i.e. low-frequency perturbation modes will be more likely to vanish).

Level of contact inhibition of the cell traction forces and long-range cell traction forces. The plots in Figs. 8 and 9 illustrate how the base-case dispersion relations displayed in Fig. 2 change when different values of the parameter λ (i.e. the level of cell-cell contact inhibition of the cell traction forces) and the parameter β (i.e. the long-range cell traction forces) are, respectively, considered. Considerations similar to those previously made about the dispersion relations obtained for increasing values of the parameters r and s apply to the case where increasing values of the parameter λ and the parameter β are considered. In addition to these considerations, the plots in Figs. 8 and 9 indicate that for small enough values of λ or β the SLS model (5) can exhibit unstable modes, which further suggests that weaker contact inhibition of cell traction forces and lower long-range cell traction forces foster pattern formation. Moreover, the plots in Fig. 9 indicate that in the asymptotic regime $\beta \rightarrow 0$ we may observe infinitely many unstable modes (i.e. $\text{Re}(\psi(k^2)) > 0$ for arbitrarily large wavenumbers), exiting the regime of physically meaningful pattern forming instabilities (Moreo et al. 2010; Perelson et al. 1986).

Cell haptotactic sensitivity and cell traction forces. The plots in Figs. 10 and 11 illustrate how the base-case dispersion relations displayed in Fig. 2 change when different values of the parameter α (i.e. the cell haptotactic sensitivity) and the parameter τ (i.e. the cell traction force) are, respectively, considered. As expected (Murray 2001), larger values of these parameters overall increase the value of $\text{Re}(\psi(k^2))$ and broaden the range of values of modes for which $\text{Re}(\psi(k^2)) > 0$, so that for large enough values of these parameters the linear viscous model (2), the Kelvin–Voigt model (3) and the SLS model (5) can exhibit unstable modes. However, sufficiently large values of τ appear to lead to singular dispersion relations (cf. the plots for the linear elastic model (1), the Maxwell model (4), and the SLS model (5) in Fig. 11), which suggests that linear stability theory may fail in the regime of high cell traction for certain constitutive models, as previously observed in (Byrne and Chaplain 1996).

Initial ECM density. The plots in Fig. 12 illustrate how the base-case dispersion relations displayed in Fig. 2 change when different values of the parameter ρ_0 (i.e. the initial ECM density) are considered. Considerations similar to those previously made about the dispersion relations obtained for increasing values of the parameter α apply to the case where increasing values of the parameter ρ_0 are considered. In addition to these considerations, the plots in Fig. 12 indicate that smaller values of the parameter ρ_0 , specifically $\rho_0 < 1$, correlate with a shift in mode selection towards lower modes (cf. the plots for the linear viscous model (2), the Maxwell model (4) and the Jeffrey model (6) in Fig. 12).

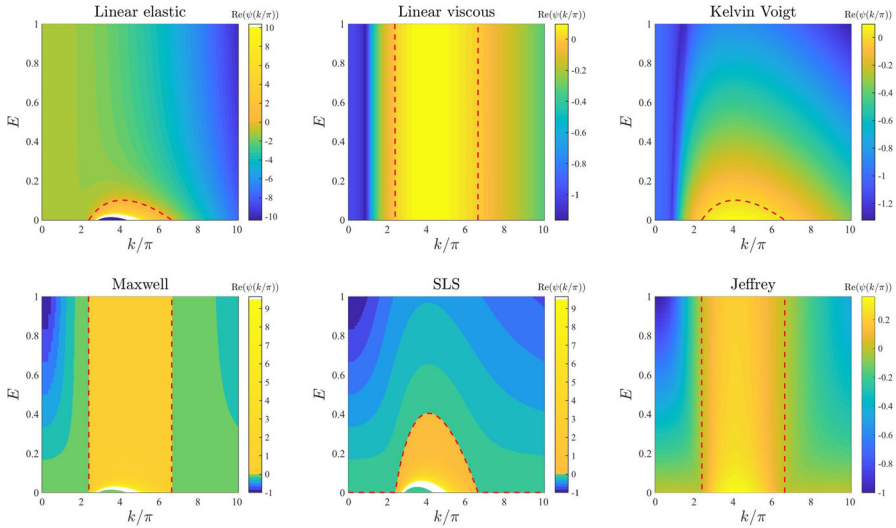


Fig. 3 Effects of varying the ECM elasticity. Dispersion relations corresponding to the stress–strain constitutive equations (1)–(6) for increasing values of the ECM elasticity, that is for $E \in [0, 1]$. The values of the other parameters are given by (26) and (27). White regions in the plots related to the linear elastic model, the Maxwell model and the SLS model correspond to $\text{Re}(\psi(k^2)) > 10$ (i.e. a vertical asymptote is present in the dispersion relation). Red dashed lines mark contour lines where $\text{Re}(\psi(k^2)) = 0$

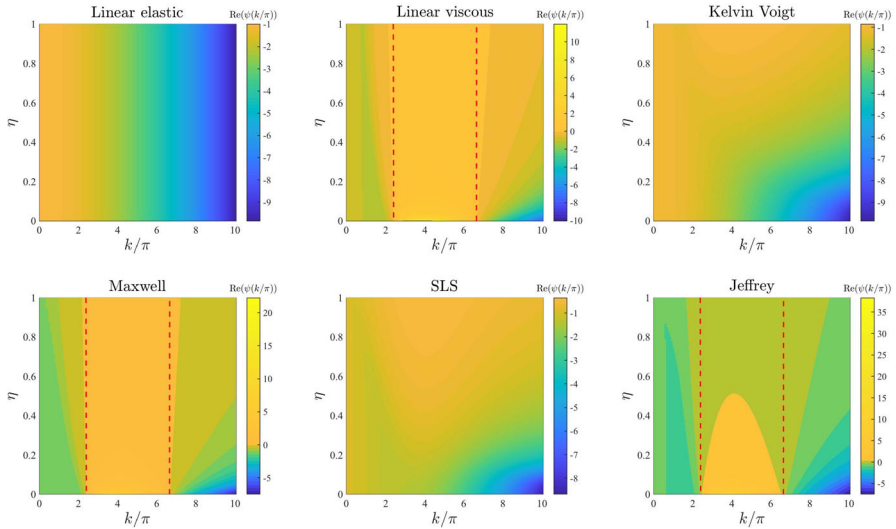


Fig. 4 Effects of varying the ECM viscosity. Dispersion relations corresponding to the stress–strain constitutive equations (1)–(6) for increasing values of the ECM viscosity, that is for $\eta \in [0, 1]$. The values of the other parameters are given by (26) and (27). Red dashed lines mark contour lines where $\text{Re}(\psi(k^2)) = 0$

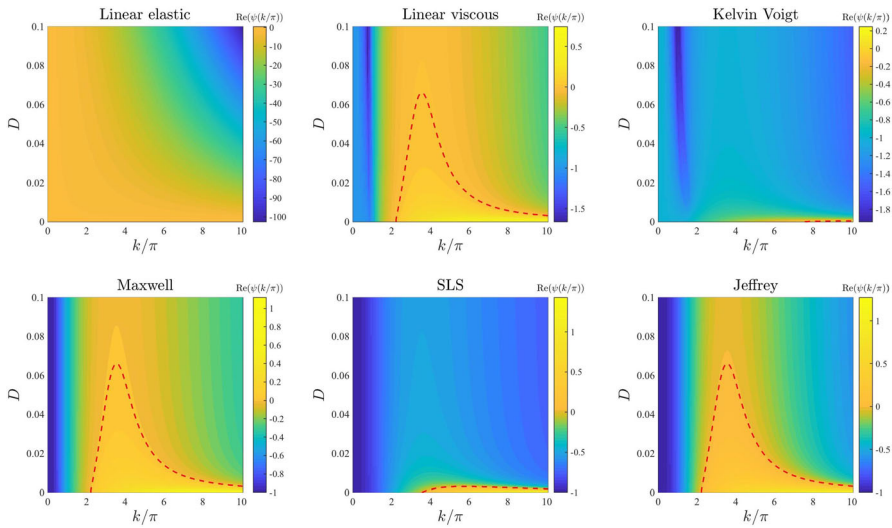


Fig. 5 Effects of varying the cell motility. Dispersion relations corresponding to the stress–strain constitutive equations (1)–(6) for increasing values of the cell motility, that is for $D \in [0, 0.1]$. The values of the other parameters are given by (26) and (27). Red dashed lines mark contour lines where $\text{Re}(\psi(k^2)) = 0$

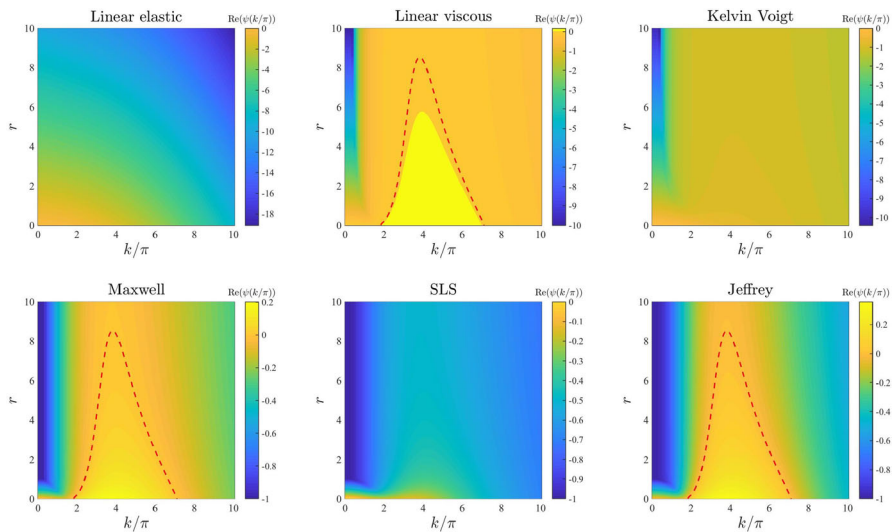


Fig. 6 Effects of varying the intrinsic growth rate of the cell density. Dispersion relations corresponding to the stress–strain constitutive equations (1)–(6) for increasing values of the intrinsic growth rate of the cell density, that is for $r \in [0, 10]$. The values of the other parameters are given by (26) and (27). Red dashed lines mark contour lines where $\text{Re}(\psi(k^2)) = 0$

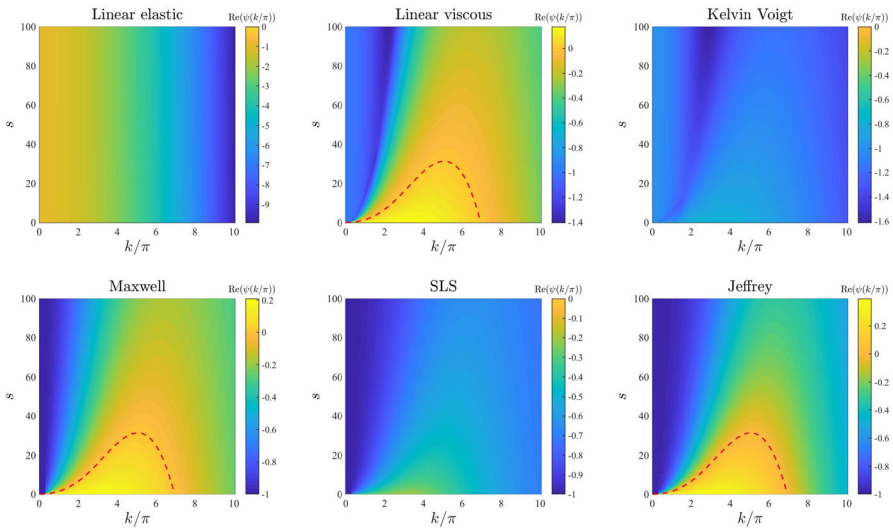


Fig. 7 Effects of varying the elasticity of the surrounding tissue. Dispersion relations corresponding to the stress–strain constitutive equations (1)–(6) for increasing values of the elasticity of the surrounding tissue, that is for $s \in [0, 100]$. The values of the other parameters are given by (26) and (27). Red dashed lines mark contour lines where $\text{Re}(\psi(k^2)) = 0$

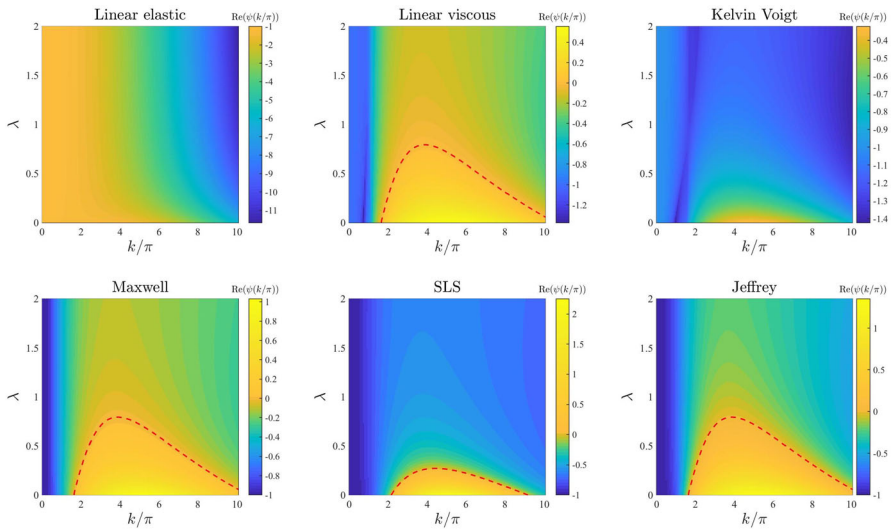


Fig. 8 Effects of varying the level of cell–cell contact inhibition of the cell traction forces. Dispersion relations corresponding to the stress–strain constitutive equations (1)–(6) for increasing levels of cell–cell contact inhibition of the cell traction forces, that is for $\lambda \in [0, 2]$. The values of the other parameters are given by (26) and (27). Red dashed lines mark contour lines where $\text{Re}(\psi(k^2)) = 0$

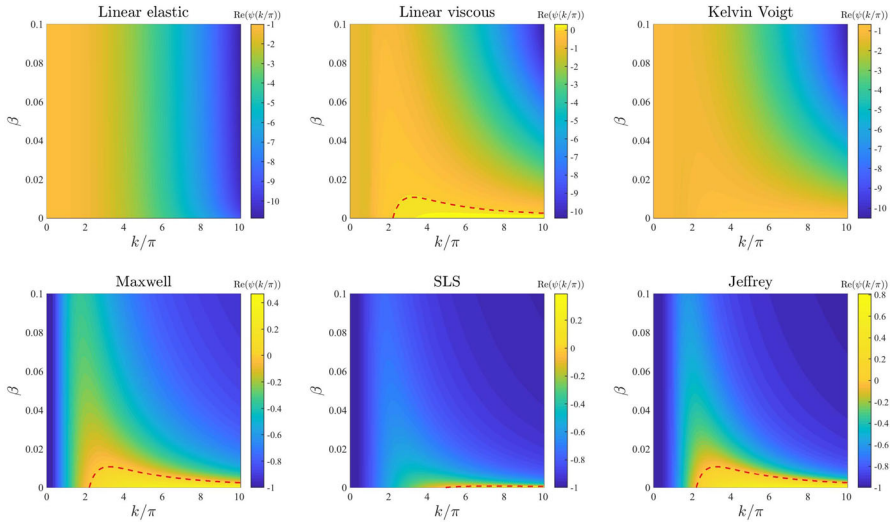


Fig. 9 Effects of varying the long-range cell traction forces. Dispersion relations corresponding to the stress–strain constitutive equations (1)–(6) for increasing long-range cell traction forces, that is for $\beta \in [0, 0.1]$. The values of the other parameters are given by (26) and (27). Red dashed lines mark contour lines where $\text{Re}(\psi(k^2)) = 0$

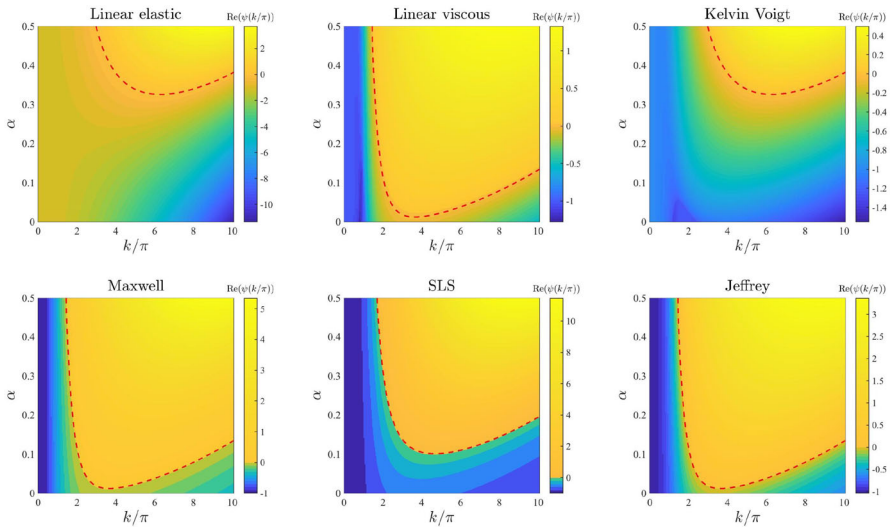


Fig. 10 Effects of varying the cell haptotactic sensitivity. Dispersion relations corresponding to the stress–strain constitutive equations (1)–(6) for increasing values of the cell haptotactic sensitivity, that is for $\alpha \in [0, 0.5]$. The values of the other parameters are given by (26) and (27). Red dashed lines mark contour lines where $\text{Re}(\psi(k^2)) = 0$

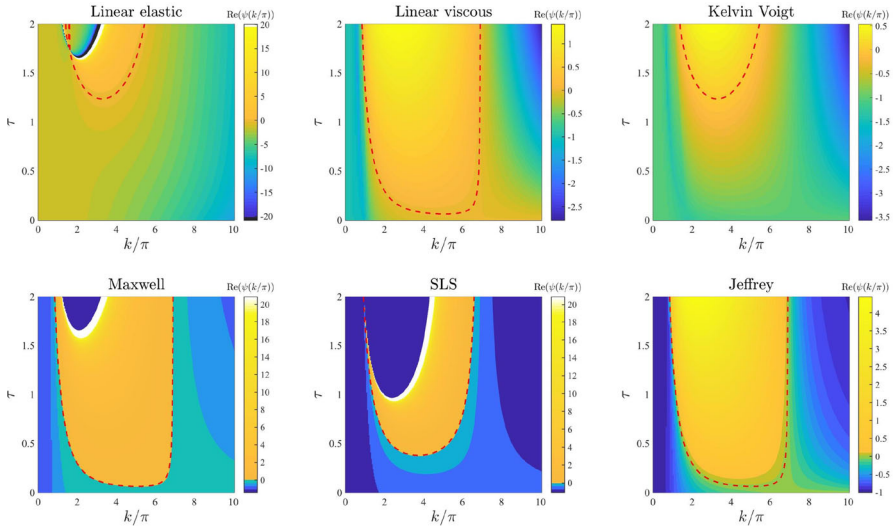


Fig. 11 Effects of varying the cell traction forces. Dispersion relations corresponding to the stress–strain constitutive equations (1)–(6) for increasing cell traction forces, that is for $\tau \in [0, 2]$. The values of the other parameters are given by (26) and (27). White and black regions in the plots related to the linear elastic model, the Maxwell model and the SLS model correspond, respectively, to $\text{Re}(\psi(k^2)) > 20$ and $\text{Re}(\psi(k^2)) < -20$ (i.e. a vertical asymptote is present in the dispersion relation). Red dashed lines mark contour lines where $\text{Re}(\psi(k^2)) = 0$

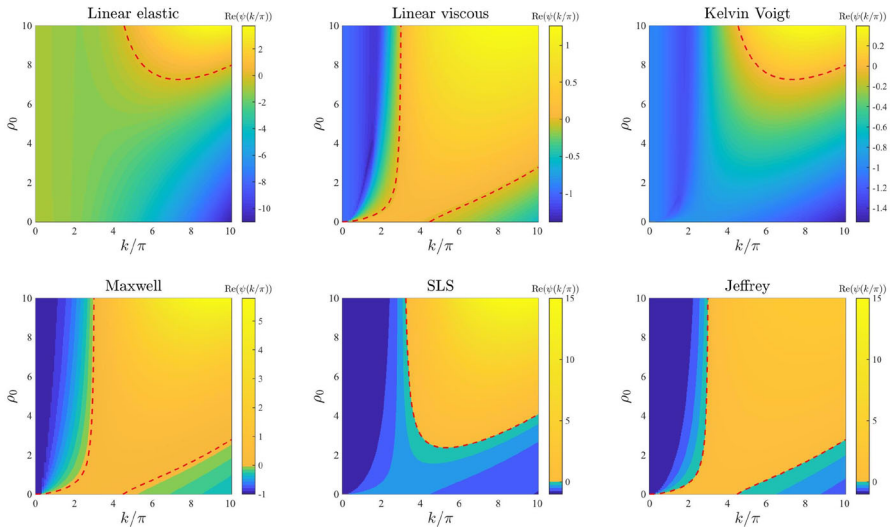


Fig. 12 Effects of varying the initial ECM density. Dispersion relations corresponding to the stress–strain constitutive equations (1)–(6) for increasing values of the initial ECM density, that is for $\rho_0 \in [0, 10]$. The values of the other parameters are given by (26) and (27). Red dashed lines mark contour lines where $\text{Re}(\psi(k^2)) = 0$

5 Numerical Simulations of a One-Dimensional Mechanical Model of Pattern Formation

In this section, we verify key results of LSA presented in Sect. 4 by solving numerically the system of PDEs (10), (11) and (16) subject to boundary conditions (17). In particular, we report on numerical solutions obtained in the case where Eq. (16) is complemented with the Kelvin–Voigt model (3) or the Maxwell model (4). A detailed description of the numerical schemes employed is provided in the Supplementary Material (see file ‘SuppInfo’).

Set-up of numerical simulations. We carry out numerical simulations using the parameter values given by (26) and (27). We choose the endpoints of the spatial domain to be $\ell = 0$ and $L = 1$, and the final time T is chosen sufficiently large so that distinct spatial patterns can be observed at the end of simulations. We consider the initial conditions

$$n(0, x) = 1 + 0.01 \epsilon(x), \quad \rho(0, x) \equiv \rho_0, \quad u(0, x) \equiv 0, \quad (28)$$

where $\epsilon(x)$ is a normally distributed random variable with mean 0 and variance 1 for every $x \in [0, 1]$. Initial conditions (28) model a scenario where random small perturbations are superimposed to the cell density corresponding to the homogeneous steady state of components $\bar{n} = 1$, $\bar{\rho} = \rho_0$ and $\bar{u} = 0$. This is the steady state considered in the LSA undertaken in Sect. 4.1. Consistent initial conditions for $\partial_t n(0, x)$, $\partial_t \rho(0, x)$ and $\partial_t u(0, x)$ are computed numerically—details provided in the Supplementary Material (see file ‘SuppInfo’). Numerical computations are performed in MATLAB.

Main results. The results obtained are summarised by the plots in Fig. 13, together with the corresponding videos provided as supplementary material. The supplementary video ‘MovS1’ displays the solution of the system of PDEs (10), (11) and (16) subject to the boundary conditions (17) and initial conditions (28) for the Kelvin–Voigt model and the Maxwell model from $t = 0$ until a steady state, displayed in Fig. 13, is reached. The supplementary videos ‘MovS2’, ‘MovS3’, and ‘MovS4’ display the solution of the same system of PDEs for the Maxwell model under alternative initial perturbations in the cell density, *i.e.* randomly distributed (‘MovS2’), periodic (‘MovS3’) or randomly perturbed periodic (‘MovS4’) initial perturbations.

The results in Fig. 13 and the supplementary video ‘MovS1’ demonstrate that, in agreement with the dispersion relations displayed in Fig. 2, for the parameter values given by (26) and (27), small randomly distributed perturbations present in the initial cell density:

- vanish in the case of the Kelvin–Voigt model, thus leading the cell density to relax to the homogeneous steady state $\bar{n} = 1$ and attain numerical equilibrium at $t = 100$ while leaving the ECM density unchanged;
- grow in the case of the Maxwell model, resulting in the formation of spatial patterns both in the cell density n and in the ECM density ρ , which attain numerical equilibrium at $t = 500$.

Notice that the formation of spatial patterns correlates with the growth of the cell-ECM displacement u . In fact, the displacement remains close to zero (*i.e.* $\sim O(10^{-11})$)

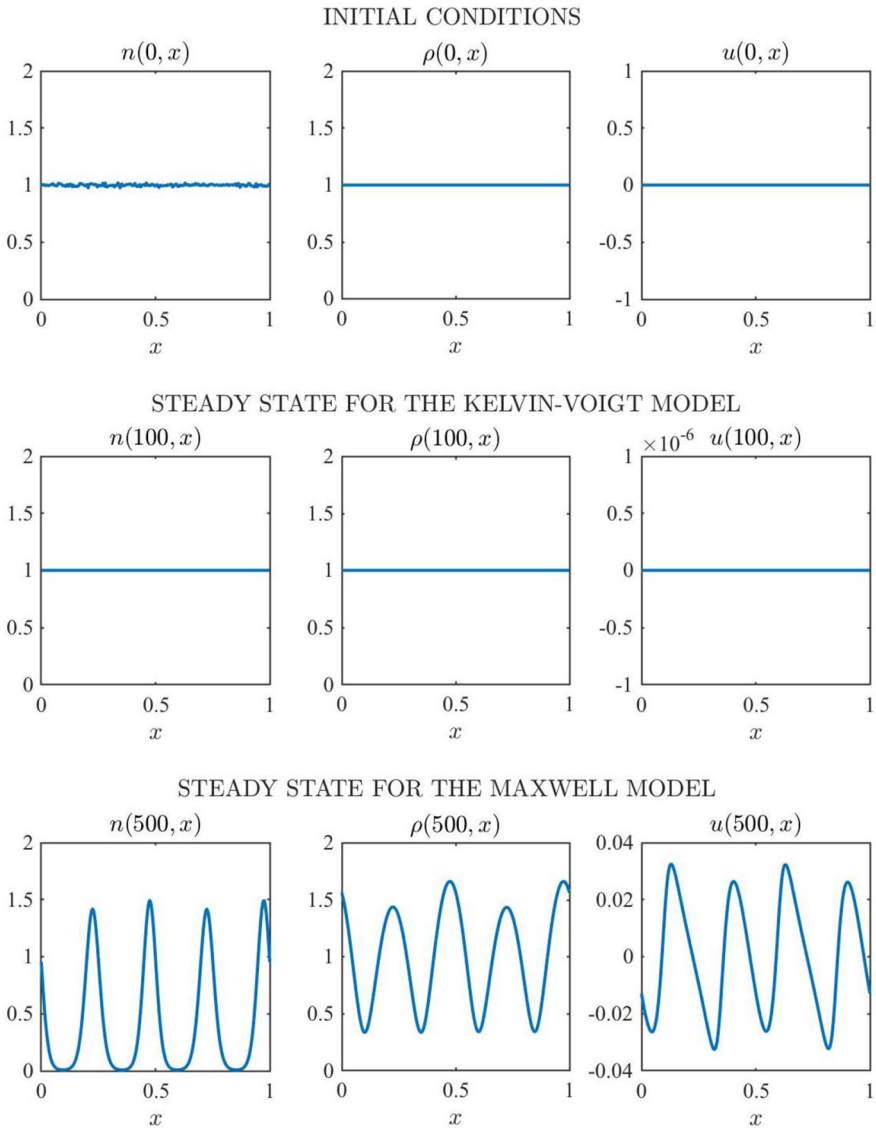


Fig. 13 Simulation results for the Kelvin–Voigt model (3) and the Maxwell model (4) under initial conditions (28). Cell density $n(t, x)$ (left), ECM density $\rho(t, x)$ (centre) and cell-ECM displacement $u(t, x)$ (right) at $t = 0$ (first row) and at steady state obtained solving numerically the system of PDEs (10), (11) and (16) complemented with the Kelvin–Voigt model (3) (second row) and with the Maxwell model (4) (third row), respectively, subject to boundary conditions (17) and initial conditions (28), for the parameter values given by (26) and (27)

for the Kelvin–Voigt model, whereas it grows with time for the Maxwell model. In addition, the steady state obtained for the Maxwell model in Fig. 13, together with those obtained when considering alternative initial perturbations (see supplementary videos ‘MovS2’, ‘MovS3’, and ‘MovS4’), demonstrate that, in agreement with the dispersion relation displayed in Fig. 2 for the Maxwell model, for the parameter values given by (26) and (27), under small perturbations in the cell density, be they randomly distributed (cf. supplementary video ‘MovS2’), randomly perturbed periodic (cf. supplementary video ‘MovS3’) or periodic (cf. supplementary video ‘MovS4’), the fourth mode is the fastest growing one within the range of unstable modes (cf. $\text{Re}(\psi(k^2)) > 0$ for k/π between 2 and 6, with $\max(\text{Re}(\psi(k^2))) \approx 4$ in Fig. 2 for the Maxwell model). In addition, the cellular pattern observed at steady state exhibits 4 large and equally spaced peaks independently of the initial perturbation (cf. supplementary videos ‘MovS1’, ‘MovS2’, ‘MovS3’, and ‘MovS4’). Moreover, all the obtained cellular patterns at steady state exhibit the same structure—up to a horizontal shift—consisting of four large peaks, independently of the initial conditions that is used (cf. left panel in the bottom row of Fig. 13 and supplementary videos ‘MovS2’, ‘MovS3’, and ‘MovS4’). This indicates robustness and consistency in the nature of the saturated nonlinear steady state under specific viscoelasticity assumptions and parameter choices.

6 Numerical Simulations of a Two-Dimensional Mechanical Model of Pattern Formation

In this section, we complement the results presented in the previous sections with the results of numerical simulations of a two-dimensional mechanical model of pattern formation in biological tissues. In particular, we report on numerical solutions obtained in the case where the two-dimensional analogue of the system of PDEs (10), (11) and (16) is complemented with a two-dimensional version of the one-dimensional Kelvin–Voigt model (3) or a two-dimensional version of the one-dimensional Maxwell model (4).

A two-dimensional mechanical model of pattern formation. The mechanical model of pattern formation defined by the system of PDEs (10), (11) and (12) posed on a two-dimensional spatial domain represented by a bounded set $\Omega \subset \mathbb{R}^2$ with smooth boundary $\partial\Omega$ reads as

$$\begin{cases} \partial_t n = \text{div} [D \nabla n - n (\alpha \nabla \rho + \partial_t \mathbf{u})] + r n(1 - n), \\ \partial_t \rho = - \text{div}(\rho \partial_t \mathbf{u}), \\ \text{div}(\boldsymbol{\sigma}_m + \boldsymbol{\sigma}_c) + \rho \mathbf{F} = 0, \end{cases} \tag{29}$$

with $t \in (0, T]$, $\mathbf{x} = (x_1, x_2)^\top \in \Omega$ and $\mathbf{u} = (u_1, u_2)^\top$. We close the system of PDEs (29) imposing the two-dimensional version of the periodic boundary conditions (17) on $\partial\Omega$. Furthermore, we use the following two-dimensional analogues of

Table 3 Relations between the parameters in the generic two-dimensional stress–strain constitutive equation (31) and those in the two-dimensional constitutive equations for the Kelvin–Voigt model and the Maxwell model.

Generic two-dimensional model	\mathbf{a}_1	\mathbf{a}_0	\mathbf{b}_1	\mathbf{b}_0	\mathbf{c}_1	\mathbf{c}_0
Kelvin–Voigt model	0	$\frac{1}{\eta}$	1	$\frac{E'}{\eta}$	ν'	$\frac{E'\nu'}{\eta}$
Maxwell model	$\frac{1}{E'}$	$\frac{1}{\eta}$	1	0	ν'	0

definitions (13) and (15)

$$\boldsymbol{\sigma}_c := \frac{\tau n}{1 + \lambda n^2} (\rho + \beta \Delta \rho) \mathbf{I} \quad \text{and} \quad \mathbf{F} := -s \mathbf{u}, \tag{30}$$

where \mathbf{I} is the identity tensor. Moreover, in analogy with the one-dimensional case, we define the stress tensor $\boldsymbol{\sigma}_m$ via the two-dimensional constitutive model that is used to represent the stress–strain relation of the ECM. In particular, we consider the following generic two-dimensional constitutive equation

$$a_1 \partial_t \boldsymbol{\sigma} + a_0 \boldsymbol{\sigma} = b_1 \partial_t \boldsymbol{\varepsilon} + b_0 \boldsymbol{\varepsilon} + c_1 \partial_t \theta \mathbf{I} + c_0 \theta \mathbf{I}. \tag{31}$$

This constitutive equation, together with the associated parameter choices reported in Table 3, summarises the two-dimensional version of the one-dimensional Kelvin–Voigt model (3) and the two-dimensional version of the one-dimensional Maxwell model (4) that are considered, which are derived in Appendix B.

Here, the strain $\boldsymbol{\varepsilon}(t, \mathbf{x})$ and the dilation $\theta(t, \mathbf{x})$ are defined in terms of the displacement $\mathbf{u}(t, \mathbf{x})$ as

$$\boldsymbol{\varepsilon} = \frac{1}{2} (\nabla \mathbf{u} + \nabla \mathbf{u}^\top) \quad \text{and} \quad \theta = \nabla \cdot \mathbf{u}. \tag{32}$$

Notice that both $\boldsymbol{\varepsilon}$ and θ reduce to $\varepsilon = \partial_x u$ in the one-dimensional case. Amongst the parameters in the stress–strain constitutive equation (31) reported in Table 3 for the two-dimensional Kelvin–Voigt and Maxwell models, η is the shear viscosity,

$$E' := \frac{E}{1 + \nu} \quad \text{and} \quad \nu' := \frac{\nu}{1 - 2\nu}, \tag{33}$$

where ν is Poisson’s ratio and E is Young’s modulus. As clarified in Appendix B, the two-dimensional Maxwell model in the form (31) holds under the simplifying assumption that the quotient between the bulk viscosity and the shear viscosity of the ECM is equal to ν' .

Set-up of numerical simulations. We solve numerically the system of PDEs (29) subject to the two-dimensional version of the periodic boundary conditions (17) and complemented with (30)-(33). Numerical simulations are carried out using the following

parameter values

$$E = 1, \quad \eta = 1, \quad D = 0.01, \quad \nu = 0.25, \quad (34)$$

$$\alpha = 0.05, \quad r = 1, \quad s = 10, \quad \lambda = 0.5, \quad \tau = 0.2 \quad \beta = 0.005, \quad (35)$$

which are chosen for illustrative purposes and are comparable with nondimensional parameter values that can be found in the extant literature (see Appendix A for further details). We choose $\Omega = [0, 1] \times [0, 1]$ and the final time T is chosen sufficiently large so that distinct spatial patterns can be observed at the end of simulations. We consider first the following two-dimensional analogue of initial conditions (28)

$$n(0, x_1, x_2) = 1 + 0.01 \epsilon(x_1, x_2), \quad \rho(0, x_1, x_2) \equiv 1, \quad \mathbf{u}(0, x_1, x_2) \equiv \mathbf{0}, \quad (36)$$

where $\epsilon(x_1, x_2)$ is a normally distributed random variable with mean 0 and variance 1 for each $(x_1, x_2) \in [0, 1] \times [0, 1]$. Consistent initial conditions for $\partial_t n(0, x_1, x_2)$, $\partial_t \rho(0, x_1, x_2)$ and $\partial_t \mathbf{u}(0, x_1, x_2)$ are computed numerically, as similarly done in the one-dimensional case, and numerical computations are performed in MATLAB with a numerical scheme analogous to that employed in the one-dimensional case—details provided in the Supplementary Material (see file ‘SuppInfo’).

Main results. The results obtained are summarised by the plots in Figures 14 and 15, together with the corresponding videos provided as supplementary material. Solutions of the system of PDEs (29), together with (30)–(33), subject to initial conditions (36) and periodic boundary conditions, for the parameter values given by (34) and (35), are calculated both for the Kelvin–Voigt model (see supplementary video ‘MovS5’) and the Maxwell model (see supplementary video ‘MovS6’) according to the parameter changes summarised in Table 3. The randomly generated initial perturbation in the cell density, together with the cell density at $t = 200$ both for the Kelvin–Voigt and the Maxwell model are displayed in Fig. 14, while the solution to the Maxwell model is plotted at a later time in Fig. 15. Overall, these results demonstrate that, in the scenarios considered here, which are analogous to those considered for the corresponding one-dimensional models, small randomly distributed perturbations present in the initial cell density (*cf.* first panel in Fig. 14):

- vanish in the case of the Kelvin–Voigt model, thus leading the cell density to relax to the homogeneous steady state $\bar{n} = 1$ and attain numerical equilibrium at $t = 260$ (*cf.* second panel of Fig. 14) while leaving the ECM density unchanged (see supplementary video ‘MovS5’);
- grow in the case of the Maxwell model, leading to the formation of spatio-temporal patterns both in the cell density n and in the ECM density ρ (*cf.* third panel of Figure 14, Fig. 15 and supplementary video ‘MovS6’), capturing spatio-temporal dynamic heterogeneity arising in the system.

Similarly to the one-dimensional case, the formation of spatial patterns correlates with the growth of the cell-ECM displacement \mathbf{u} . In fact, the displacement remains close to zero (*i.e.* $\sim O(10^{-11})$) for the Kelvin–Voigt model (see supplementary video ‘MovS5’), whereas it grows with time for the Maxwell model (see Figure 15 and supplementary video ‘MovS6’).

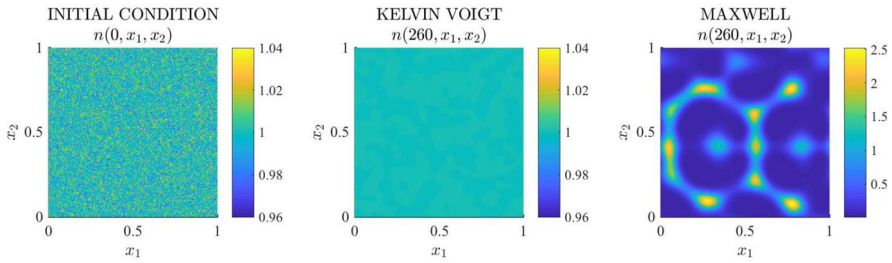


Fig. 14 Simulation results for the two-dimensional Kelvin–Voigt and Maxwell models (31) under initial conditions (36). Cell density $n(t, x_1, x_2)$ at $t = 0$ (left panel) and at $t = 260$ for the Kelvin–Voigt model (central panel) and the Maxwell model (right panel) obtained solving numerically the system of PDEs (29) subject to the two-dimensional version of the periodic boundary conditions (17) and initial conditions (36), complemented with (30)–(33), for the parameter values given by (34) and (35)

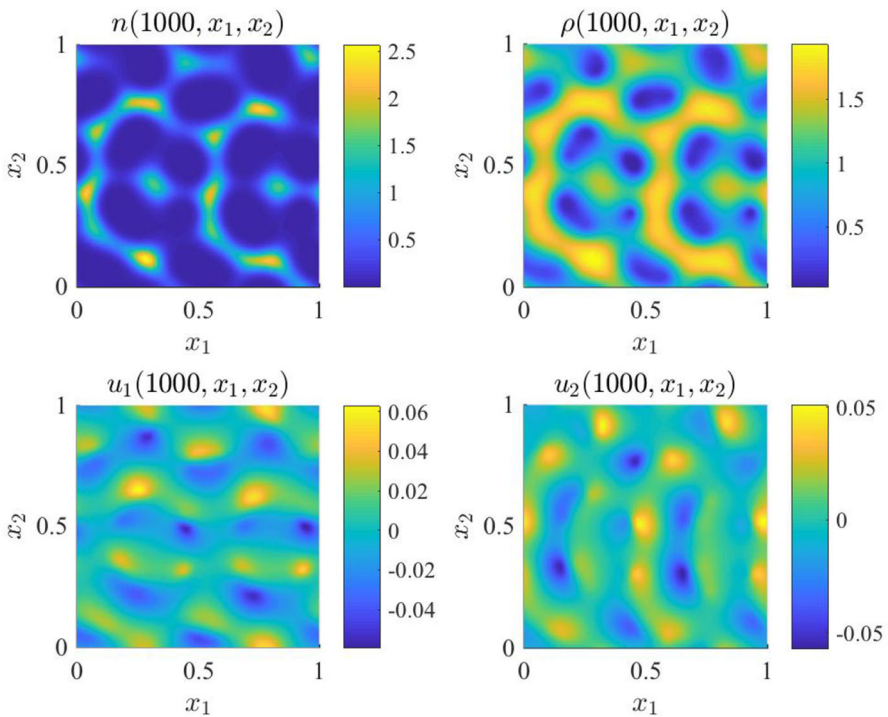


Fig. 15 Simulation results for the two-dimensional Maxwell model (31) under initial conditions (36). Cell density $n(t, x_1, x_2)$ (top row, left panel), ECM density $\rho(t, x_1, x_2)$ (top row, right panel), first and second components of the cell–ECM displacement $\mathbf{u}(t, x_1, x_2)$ (bottom row, left panel and right panel, respectively) at $t = 1000$ for the Maxwell model obtained solving numerically the system of PDEs (29) subject to the two-dimensional version of the periodic boundary conditions (17) and initial conditions (36), complemented with (30)–(33), for the parameter values given by (34) and (35). The random initial perturbation of the cell density is displayed in the left panel of Fig. 14

7 Conclusions and Research Perspectives

Conclusions. We have investigated the pattern formation potential of different stress–strain constitutive equations for the ECM within a one-dimensional mechanical model of pattern formation in biological tissues formulated as the system of implicit PDEs (10), (11), and (16).

The results of linear stability analysis undertaken in Sect. 4 and the dispersion relations derived therefrom support the idea that fluid-like stress–strain constitutive equations (*i.e.* the linear viscous model (2), the Maxwell model (4) and the Jeffrey model (6)) have a pattern formation potential much higher than solid-like constitutive equations (*i.e.* the linear elastic model (1), the Kelvin–Voigt model (3) and the SLS model (5)). This is confirmed by the results of numerical simulations presented in Sect. 5, which demonstrate that, all else being equal, spatial patterns emerge in the case where the Maxwell model (4) is used to represent the stress–strain relation of the ECM, while no patterns are observed when the Kelvin–Voigt model (3) is employed. In addition, the structure of the spatial patterns presented in Sect. 5 for the Maxwell model (4) is consistent with the fastest growing mode predicted by linear stability analysis. In Sect. 6, as an illustrative example, we have also reported on the results of numerical simulations of a two-dimensional version of the model, which is given by the system of PDEs (29) complemented with the two-dimensional Kelvin–Voigt and Maxwell models (31). These results demonstrate that key features of spatial pattern formation observed in one spatial dimension carry through when two spatial dimensions are considered, thus conferring additional robustness to the conclusions of our work.

Our findings corroborate the conclusions of Byrne and Chaplain (1996), suggesting that prior studies on mechanochemical models of pattern formation relying on the Kelvin–Voigt model of viscoelasticity may have underestimated the pattern formation potential of biological tissues and advocating the need for further empirical work to acquire detailed quantitative information on the mechanical properties of single components of the ECM in different biological tissues, in order to furnish such models with stress–strain constitutive equations for the ECM that provide a more faithful representation of tissue rheology, *cf.* Fung (1993).

Research perspectives. The dispersion relations given in Sect. 4 indicate that there may be parameter regimes whereby solid-like constitutive models of linear viscoelasticity give rise to dispersion relations which exhibit a range of unstable modes, while the dispersion relations obtained using fluid-like constitutive models exhibit singularities, exiting the regime of validity of linear stability analysis. In this regard, it would be interesting to consider extended versions of the mechanical model of pattern formation defined by the system of PDEs (10), (11) and (16), in order to re-enter the regime of validity of linear stability analysis for the same parameter regimes and verify that in such regimes all constitutive models can produce patterns. For instance, it is known that including long-range effects, such as long-range diffusion or long-range haptotaxis, can promote the formation of stable spatial patterns (Moreo et al. 2010; Oster et al. 1983), which could be explored through nonlinear stability analysis, as previously done for the case in which the stress–strain relation of the ECM is represented by the Kelvin–Voigt model (Cruywagen and Murray 1992; Lewis and Murray 1991; Maini

and Murray 1988). In particular, weakly nonlinear analysis could provide information on the existence and stability of saturated nonlinear steady states, supercritical bifurcations or subcritical bifurcations, which may exist even when the homogeneous steady states are stable to small perturbations according to linear stability analysis (Cross and Greenside 2009). Nonlinear analysis would further enable exploring the existence of possible differences in the spatial patterns obtained when different stress–strain constitutive equations for the ECM are used—such as amplitude of patterns, perturbation mode selection, and geometric structure in two spatial dimensions. In particular, the base-case dispersion relations given in Sect. 4 for different fluid-like models of viscoelasticity displayed the same range of unstable modes. This suggests that the investigation of similarities and differences in mode selection between the various models of viscoelasticity could yield interesting results. It would also be interesting to construct numerical solutions for the mechanical model defined by the system of PDEs (10), (11) and (16) complemented with the Jeffrey model (6). For this to be done, suitable extensions of the numerical schemes presented in the Supplementary Material (see file ‘SuppInfo’) need to be developed.

It would also be relevant to systematically assess the pattern formation potential of different constitutive models of viscoelasticity in two spatial dimensions. This would require to relax the simplifying assumption (A.4) on the shear and bulk viscosities of the ECM, which we have used to derive the two-dimensional Maxwell model in the form of (31), and, more in general, to find analytically and computationally tractable stress–strain–dilation relations, which still remains an open problem (Birman et al. 2002; Haghghi-Yazdi and Lee-Sullivan 2011). In order to solve this problem, new methods of derivation and parameterisation for constitutive models of viscoelasticity might need to be developed (Valtorta and Mazza 2005).

As previously mentioned, the values of the model parameters used in this paper have been chosen for illustrative purposes only. Hence, it would be useful to re-compute the dispersion relations and the numerical solutions presented here for a calibrated version of the model based on real biological data. On a related note, there exists a variety of interesting applications that could be explored by varying parameter values in the generic constitutive equation (16) both in space and time. For instance, cell monolayers appear to exhibit solid-like behaviours on small time scales, whereas they exhibit fluid-like behaviours on longer time scales (Tlili et al. 2018), and spatio-temporal changes in basement membrane components are known to affect structural properties of tissues during development or ageing, as well as in a number of genetic and autoimmune diseases (Khalilgharibi and Mao 2021). Amongst these, remarkable examples are Alport’s syndrome, characterised by changes in collagen IV network due to genetic mutations associated with the disease, diabetes mellitus, whereby high levels of glucose induce significant basement membrane turnover, and cancer. In particular, cancer-associated fibrosis is a disease characterised by an excessive production of collagen, elastin, and proteoglycans, which directly affects the structure of the ECM resulting in alterations of viscoelastic tissue properties (Ebihara et al. 2000). Such alterations in the ECM may facilitate tumour invasion and angiogenesis. Considering a calibrated mechanical model of pattern formation in biological tissues, whereby the values of the parameters in the stress–strain constitutive equation for the ECM change during fibrosis progression, may shed new light on the existing connections

between structural changes in the ECM components and higher levels of malignancy in cancer (Chandler et al. 2019; Park et al. 2001).

Supplementary Information The online version contains supplementary material available at <https://doi.org/10.1007/s11538-021-00912-5>.

Acknowledgements The authors wish to thank the two anonymous Reviewers for their thoughtful and constructive feedback on the manuscript. MAJC gratefully acknowledges the support of EPSRC Grant No. EP/S030875/1 (EPSRC SoftMech[^]MP Centre-to-Centre Award).

Declarations

Conflicts of interest The authors declare that they have no conflict of interest.

Open Access This article is licensed under a Creative Commons Attribution 4.0 International License, which permits use, sharing, adaptation, distribution and reproduction in any medium or format, as long as you give appropriate credit to the original author(s) and the source, provide a link to the Creative Commons licence, and indicate if changes were made. The images or other third party material in this article are included in the article's Creative Commons licence, unless indicated otherwise in a credit line to the material. If material is not included in the article's Creative Commons licence and your intended use is not permitted by statutory regulation or exceeds the permitted use, you will need to obtain permission directly from the copyright holder. To view a copy of this licence, visit <http://creativecommons.org/licenses/by/4.0/>.

A Choice of the Parameter Values for the Baseline Parameter Sets (26)–(27) and (34)–(35)

In order not to limit the conclusions of our work by selecting a specific biological scenario, we identified possible ranges of values for each parameter of our model on the basis of the existing literature on mechanochemical models of pattern formation and then define our baseline parameter set by selecting values in the middle of such ranges. In the sensitivity analysis presented in Section 4.2, we then consider the effect of varying the parameter values within an appropriate range. We first consider the parameters appearing in equations (10), (11) and (16), as well as in the initial conditions (28) and then consider additional parameters appearing in the two-dimensional system (29)–(33), and the associated initial conditions (36).

Parameters in the balance equation (10) Nondimensional parameter values for the cell motility coefficient D in the literature appear as low as $D = 10^{-8}$ (Gilmore et al. 2012), and as high as $D = 10$ (Murray and Oster 1984b), but are generally taken in the range $[10^{-5}, 1]$ (Bentil and Murray 1991; Byrne and Preziosi 2003; Cruywagen and Murray 1992; Ferrenq et al. 1997; Maini et al. 2002; Murray et al. 1988; Namy et al. 2004; Olsen et al. 1995; Perelson et al. 1986). Hence, we take $D = 0.01$ for our baseline parameter set. The nondimensional haptotactic sensitivity of cells α takes values in the range $[10^{-5}, 5]$ (Bentil and Murray 1991; Cruywagen and Murray 1992; Gilmore et al. 2012; Murray et al. 1988; Namy et al. 2004; Olsen et al. 1995; Perelson et al. 1986), and we take $\alpha = 0.05$ for our baseline parameter set. While most authors ignore cell proliferation dynamics, *i.e.* consider $r = 0$ (Ambrosi et al. 2005; Byrne and Preziosi 2003; Gilmore et al. 2012; Murray et al. 1988; Perelson et al. 1986), when present, the rate of cell proliferation takes nondimensional value in the range $[0.02, 5]$

(Cruywagen and Murray 1992; Olsen et al. 1995; Perelson et al. 1986). Hence, we choose $r = 1$ for our baseline parameter set.

Parameters in the balance equation (11) While no parameters appear in the balance equation (11), the value of the parameter ρ_0 introduced in Sect. 4 as the spatially homogenous steady state $\bar{\rho} = \rho_0$, and successively specified to be the initial ECM density in (28) for our numerical simulations, stems from neglected terms in Eq. (11). With the exception of Cruywagen and Murray (1992) and Maini et al. (2002) who, respectively, have $\rho_0 = 100.2$ and $\rho_0 = 0.1$, this parameter is usually taken to be $\rho_0 = 1$ in mechanochemical models ignoring additional ECM dynamics (Bentil and Murray 1991; Cruywagen and Murray 1992; Harris et al. 1981; Manoussaki 2003; Moreo et al. 2010; Murray and Oster 1984a,b; Olsen et al. 1995; Oster et al. 1983; Perelson et al. 1986). This is generally justified by assuming the steady state ρ_0 of equation (11) that is introduced by the additional term, say $S(n, \rho)$, is itself used to nondimensionalise ρ , before assuming the dynamics modelled by $S(n, \rho)$ to occur on a much slower timescale than convection driven by the cell-ECM displacement, thus neglecting this term (Murray 2001, p.328), resulting in the nondimensional parameter $\hat{\rho}_0 = 1$. Hence, we take $\rho_0 = 1$.

Parameters in the force balance Eq. (16) The elastic modulus, or Young modulus, E is usually itself used to nondimensionalise the other parameters in the dimensional correspondent of equation (16) and, therefore, does not appear in the nondimensional system (Bentil and Murray 1991; Gilmore et al. 2012; Murray and Oster 1984b,b; Murray et al. 1988; Olsen et al. 1995; Perelson et al. 1986). This corresponds to the nondimensional value $E = 1$, which is what we take for our baseline parameter set. The viscosity coefficient η has been taken with nondimensional values in low orders of magnitude, such as $\eta \sim 10^{-3} - 10^{-1}$ (Bentil and Murray 1991; Cruywagen and Murray 1992; Gilmore et al. 2012; Perelson et al. 1986), as well as in high orders of magnitude, such as $\eta \sim 10^2 - 10^3$ (Gilmore et al. 2012; Olsen et al. 1995). It is, however, generally taken to be $\eta = 1$ (Bentil and Murray 1991; Byrne and Chaplain 1996; Cruywagen and Murray 1992; Murray and Oster 1984b; Murray et al. 1988; Perelson et al. 1986), which is what we choose for our baseline parameter set. When the constitutive model includes two elastic moduli, *i.e.* for the SLS model (5), or two viscosity coefficients, *i.e.* for the Jeffrey model (6), we take $E_1 = E_2 = E/2 = 0.5$ and $\eta_1 = \eta_2 = \eta/2 = 0.5$ as done by Alonso et al. (2017). The cell traction parameter τ takes nondimensional values spanning many orders of magnitude: it can be found as low as $\tau = 10^{-5}$ (Ferrenq et al. 1997) and as high as $\tau = 10$ (Bentil and Murray 1991; Cruywagen and Murray 1992; Perelson et al. 1986), but it is generally taken to be of order $\tau \sim 1$ (Bentil and Murray 1991; Byrne and Chaplain 1996; Gilmore et al. 2012; Murray et al. 1988; Perelson et al. 1986) and many works consider $\tau \sim 10^{-2} - 10^{-1}$ (Byrne and Chaplain 1996; Ferrenq et al. 1997; Murray and Oster 1984b; Olsen et al. 1995). Hence, for our baseline parameter set we choose $\tau = 0.2$. The cell-cell contact inhibition parameter λ generally takes nondimensional values in the range $[10^{-2}, 1]$ (Bentil and Murray 1991; Byrne and Chaplain 1996; Murray et al. 1988; Perelson et al. 1986), so we choose $\lambda = 0.5$ for our baseline parameter set. The long-range cell traction parameter β , when present, takes nondimensional values in the range $[10^{-3}, 10^{-2}]$ (Bentil and Murray 1991; Cruywagen and Murray 1992; Gilmore et al. 2012; Moreo et al. 2010; Murray et al. 1988; Perelson et al. 1986) so we choose $\beta = 0.005$ for our baseline

parameter set. The elasticity of the external elastic substratum s , which is sometimes ignored or substituted with a viscous drag, has been taken to have nondimensional values as low as $s \in [10^{-1}, 1]$ (Byrne and Chaplain 1996; Murray and Oster 1984b; Olsen et al. 1995) but is generally chosen in the range $[10, 400]$ (Bentil and Murray 1991; Gilmore et al. 2012; Murray et al. 1988; Perelson et al. 1986). Hence, we take $s = 10$ for our baseline parameter set.

Parameters in the 2D system (29)–(33) For the parameters in the 2D system (29)–(33) and initial condition (36) that also appear in the equations (10), (11), (16) and initial conditions (28), we make use of the same nondimensional values selected in the one-dimensional case (see previous paragraphs). The Poisson ratio ν , which can only take values in the range $[0.1, 0.45]$, has been estimated to be in the range $[0.2, 0.3]$ for the biological tissue considered in mechanochemical models in the current literature (Ambrosi et al. 2005; Cruywagen and Murray 1992; Manoussaki 2003; Moreo et al. 2010). Hence, we choose $\nu = 0.25$ for our baseline parameter set. This results in $E' = E/(1 + \nu) = 0.8$ and $\nu' = \nu/(1 - 2\nu) = 0.5$ according to definitions (33). In addition, under the simplifying assumption (A.4) introduced in Appendix B, the bulk viscosity takes the value $\mu = \nu'\eta = 0.5\eta = 0.5$, which is in agreement with the fact that the bulk and shear viscosities are usually assumed to take values of a similar order of magnitude in the extant literature (Ambrosi et al. 2005; Manoussaki 2003; Moreo et al. 2010; Murray 2003).

B Derivation of the Two-Dimensional Kelvin–Voigt and Maxwell Models (31)

Landau & Lifshitz derived from first principles the stress–strain relations that give the two-dimensional versions of the linear elastic model (1) and of the linear viscous model (2) in isotropic materials (Landau and Lifshitz 1970), which read, respectively, as

$$\boldsymbol{\sigma}_e = \frac{E}{1 + \nu} \left(\boldsymbol{\varepsilon}_e + \frac{\nu}{1 - 2\nu} \theta_e \mathbf{I} \right) \quad \text{and} \quad \boldsymbol{\sigma}_v = \eta \partial_t \boldsymbol{\varepsilon}_v + \mu \partial_t \theta_v \mathbf{I}. \quad (\text{A.1})$$

Here, E is Young's modulus, ν is Poisson's ratio, \mathbf{I} is the identity tensor, η is the shear viscosity and μ is the bulk viscosity. Moreover, $\boldsymbol{\varepsilon}_e$ and θ_e are the strain and dilation under a purely elastic deformation \mathbf{u}_e while $\boldsymbol{\varepsilon}_v$ and θ_v are the strain and dilation under a purely viscous deformation \mathbf{u}_v , which are all defined via (32).

In the case of a linearly viscoelastic material satisfying Kelvin–Voigt model, the two-dimensional analogue of (3) is simply given by

$$\boldsymbol{\sigma} = \boldsymbol{\sigma}_e + \boldsymbol{\sigma}_v = E' \boldsymbol{\varepsilon} + E' \nu' \theta \mathbf{I} + \eta \partial_t \boldsymbol{\varepsilon} + \mu \partial_t \theta \mathbf{I}. \quad (\text{A.2})$$

Here, E' and ν' are defined via (33) and there is no distinction between the strain or dilation associated with each component (*i.e.* $\boldsymbol{\varepsilon} = \boldsymbol{\varepsilon}_e = \boldsymbol{\varepsilon}_v$ and $\theta = \theta_e = \theta_v$), as the viscous and elastic components are connected in parallel. This is the stress–strain constitutive equation that is typically used to describe the contribution to the stress of

the cell-ECM system coming from the ECM in two-dimensional mechanochemical models of pattern formation (Cruywagen and Murray 1992; Ferrenq et al. 1997; Javierre et al. 2009; Maini and Murray 1988; Manoussaki 2003; Murray 2001; Murray et al. 1988; Murray and Oster 1984a, b; Murray et al. 1983; Olsen et al. 1995; Oster et al. 1983; Perelson et al. 1986).

On the other hand, deriving the two-dimensional analogues of Maxwell model (4), of the SLS model (5) and of the Jeffrey model (6) is more complicated due to the presence of elements connected in series. In the case of Maxwell model, using the fact that the overall strain and dilation will be distributed over the different components (i.e. $\boldsymbol{\varepsilon} = \boldsymbol{\varepsilon}_e + \boldsymbol{\varepsilon}_v$ and $\theta = \theta_e + \theta_v$) along with the fact that the stress on each component will be the same as the overall stress (i.e. $\boldsymbol{\sigma} = \boldsymbol{\sigma}_e = \boldsymbol{\sigma}_v$), one finds

$$\frac{1}{\eta} \boldsymbol{\sigma} + \frac{1}{E'} \partial_t \boldsymbol{\sigma} = \partial_t \boldsymbol{\varepsilon} + \nu' \partial_t \theta \mathbf{I} + \left(\frac{\mu}{\eta} - \nu' \right) \partial_t \theta_v \mathbf{I}, \tag{A.3}$$

with E' and ν' being defined via (33). Under the simplifying assumption that

$$\frac{\mu}{\eta} = \nu' \tag{A.4}$$

the stress–strain constitutive equation (A.3) can be rewritten in the form given by the generic two-dimensional constitutive equation (31) under the parameter choices reported in Table 3. Dividing (A.2) by η , under the simplifying assumption (A.4), the stress–strain constitutive equation for the Kelvin–Voigt model (A.2) can be rewritten as

$$\frac{1}{\eta} \boldsymbol{\sigma} = \frac{E'}{\eta} \boldsymbol{\varepsilon} + \frac{E' \nu'}{\eta} \theta \mathbf{I} + \partial_t \boldsymbol{\varepsilon} + \nu' \partial_t \theta \mathbf{I},$$

which is in the form given by the generic two-dimensional constitutive equation (31) under the parameter choices reported in Table 3.

References

Alonso S, Radszuweit M, Engel H, Bär M (2017) Mechanochemical pattern formation in simple models of active viscoelastic fluids and solids. *J Phys D Appl Phys* 50(43):434004

Ambrosi D, Bussolino F, Preziosi L (2005) A review of vasculogenesis models. *J Theor Med* 6(1):1–19

Bard J, Lauder I (1974) How well does turing’s theory of morphogenesis work? *J Theor Biol* 45(2):501–531

Barocas VH, Moon AG, Tranquillo RT (1995) The fibroblast-populated collagen microsphere assay of cell traction force—part 2: measurement of the cell traction parameter. *J Biomech Eng* 117(2):161–170

Barocas, V. H., Tranquillo, R. T., 1994. Biphasic theory and in vitro assays of cell-fibril mechanical interactions in tissue-equivalent gels. In: *Cell Mechanics and Cellular Engineering*. Springer, pp 185–209

Bentil DE, Murray JD (1991) Pattern selection in biological pattern formation mechanisms. *Appl Math Lett* 4(3):1–5

Bilston LE, Liu Z, Phan-Thien N (1997) Linear viscoelastic properties of bovine brain tissue in shear. *Biorheology* 34(6):377–385

Birman VB, Binienda WK, Townsend G (2002) 2d maxwell model. *J Macromol Sci Part B* 41(2):341–356

Bischoff JE, Arruda EM, Grosh K (2004) A rheological network model for the continuum anisotropic and viscoelastic behavior of soft tissue. *Biomech Model Mechanobiol* 3(1):56–65

- Brinkmann F, Mercker M, Richter T, Marciniak-Czochra A (2018) Post-turing tissue pattern formation: advent of mechanochemistry. *PLoS Comput Biol* 14(7):e1006259
- Byrne H, Preziosi L (2003) Modelling solid tumour growth using the theory of mixtures. *Math Med Biol J IMA* 20(4):341–366
- Byrne HM, Chaplain MAJ (1996) The importance of constitutive equations in mechanochemical models of pattern formation. *Appl Math Lett* 9(6):85–90
- Castets V, Dulos E, Boissonade J, De Kepper P (1990) Experimental evidence of a sustained standing Turing-type nonequilibrium chemical pattern. *Phys Rev Lett* 64(24):2953
- Chandler C, Liu T, Buckanovich R, Coffman L (2019) The double edge sword of fibrosis in cancer. *Trans Res* 209:55–67
- Cross M, Greenside H (2009) Pattern formation and dynamics in nonequilibrium systems. Cambridge University Press, Cambridge
- Cruywagen GC, Murray JD (1992) On a tissue interaction model for skin pattern formation. *J Nonlinear Sci* 2(2):217–240
- Ebihara T, Venkatesan N, Tanaka R, Ludwig MS (2000) Changes in extracellular matrix and tissue viscoelasticity in bleomycin-induced lung fibrosis: Temporal aspects. *Am J Respirat Crit Care Med* 162(4):1569–1576
- Ferrenq I, Tranqui L, Vailhe B, Gumery PY, Tracqui P (1997) Modelling biological gel contraction by cells: mechanocellular formulation and cell traction force quantification. *Acta Biotheoretica* 45(3–4):267–293
- Findley WN, Lai JS, Onaran K (1976) Creep and relaxation of nonlinear viscoelastic materials—with an introduction to linear viscoelasticity. Dover Publications
- Fung YC (1993) Biomechanics mechanical properties of living tissues, 2nd edn. Springer, New York
- Gierer A, Meinhardt H (1972) A theory of biological pattern formation. *Kybernetik* 12:30–39
- Gilmore SJ, Vaughan BL Jr, Madzvamuse A, Maini PK (2012) A mechanochemical model of striae distensae. *Math Biosci* 240(2):141–147
- Haghighi-Yazdi M, Lee-Sullivan P (2011) Modeling linear viscoelasticity in glassy polymers using standard rheological models
- Harris AK (1984) Tissue culture cells on deformable substrata: biomechanical implications. *J Biomech Eng* 106(1):19–24
- Harris AK, Stopak D, Wild P (1981) Fibroblast traction as a mechanism for collagen morphogenesis. *Nature* 290(5803):249–251
- Huang Y-P, Zheng Y-P, Leung S-F (2005) Quasi-linear viscoelastic properties of fibrotic neck tissues obtained from ultrasound indentation tests in vivo. *Clin Biomech* 20(2):145–154
- Javierre E, Moreo P, Doblaré M, García-Aznar JM (2009) Numerical modeling of a mechano-chemical theory for wound contraction analysis. *Int J Solids Struct* 46(20):3597–3606
- Jernvall J, Newman SA et al (2003) Mechanisms of pattern formation in development and evolution. *Development* 130(10):2027–2037
- Khalilgharibi N, Mao Y (2021) To form and function: on the role of basement membrane mechanics in tissue development, homeostasis and disease. *Open Biol* 11(2):200360
- Kondo S, Asai R (1995) A reaction-diffusion wave on the skin of the marine angelfish pomacanthus. *Nature* 376(6543):765–768
- Landau LD, Lifshitz EM (1970) Theory of elasticity. Pergamon Press, Cambridge
- Lewis MA, Murray JD (1991) Analysis of stable two-dimensional patterns in contractile cytotel. *J Nonlinear Sci* 1(3):289–311
- Liu Z, Bilston L (2000) On the viscoelastic character of liver tissue: experiments and modelling of the linear behaviour. *Biorheology* 37(3):191–201
- Maini P, Painter K, Chau HP (1997) Spatial pattern formation in chemical and biological systems. *J Chem Soc Faraday Trans* 93(20):3601–3610
- Maini PK (2005) Morphogenesis, biological. In: Scott A (ed) Morphogenesis. Routledge, Biological, Encyclopedia of Nonlinear Science, pp 587–589
- Maini PK, Murray JD (1988) A nonlinear analysis of a mechanical model for biological pattern formation. *SIAM J Appl Math* 48(5):1064–1072
- Maini PK, Olsen L, Sherratt JA (2002) Mathematical models for cell-matrix interactions during dermal wound healing. *Int J Bifurc Chaos* 12(09):2021–2029
- Maini PK, Woolley TE (2019) The Turing model for biological pattern formation. In: The dynamics of biological systems. Springer, pp 189–204

- Maini PK, Woolley TE, Baker RE, Gaffney EA, Lee SS (2012) Turing's model for biological pattern formation and the robustness problem. *Interface Focus* 2(4):487–496
- Manoussaki D (2003) A mechanochemical model of angiogenesis and vasculogenesis. *ESAIM Math Modell Numer Anal* 37(4):581–599
- Mase GE (1970) *Continuum mechanics*. McGraw-Hill, New York
- Meinhardt H (1982) *Models of biological pattern formation*. Academic Press, London
- Meinhardt H (2009) *The algorithmic beauty of sea shells*. Springer, Berlin
- Moon AG, Tranquillo RT (1993) Fibroblast-populated collagen microsphere assay of cell traction force: Part 1. continuum model. *AIChe J* 39(1):163–177
- Moreo P, Gaffney EA, Garcia-Aznar JM, Doblaré M (2010) On the modelling of biological patterns with mechanochemical models: insights from analysis and computation. *Bull Math Biol* 72(2):400–431
- Murray JD (1981) A pre-pattern formation mechanism for animal coat markings. *J Theor Biol* 88:161–199
- Murray JD (2001) *Mathematical biology. II Spatial models and biomedical applications* {Interdisciplinary Applied Mathematics V. 18}. Springer, New York Incorporated New York
- Murray JD (2003) On the mechanochemical theory of biological pattern formation with application to vasculogenesis. *Comptes Rendus Biologies* 326(2):239–252
- Murray JD, Maini PK (1986) *A new approach to the generation of pattern and form in embryology*. Scientific Programme, Oxford
- Murray JD, Maini PK (1989) Pattern formation mechanisms—a comparison of reaction-diffusion and mechanochemical models. In: *Cell to Cell Signalling*. Elsevier, pp 159–170
- Murray JD, Maini PK, Tranquillo RT (1988) Mechanochemical models for generating biological pattern and form in development. *Phys Rep* 171(2):59–84
- Murray JD, Oster GF (1984a) Cell traction models for generating pattern and form in morphogenesis. *J Math Biol* 19(3):265–279
- Murray JD, Oster GF (1984b) Generation of biological pattern and form. *Math Med Biol J IMA* 1(1):51–75
- Murray JD, Oster GF, Harris AK (1983) A mechanical model for mesenchymal morphogenesis. *J Math Biol* 17(1):125–129
- Namy P, Ohayon J, Tracqui P (2004) Critical conditions for pattern formation and in vitro tubulogenesis driven by cellular traction fields. *J Theor Biol* 227(1):103–120
- Nargess K, Yanlan M (2021) To form and function: on the role of basement membrane mechanics in tissue development, homeostasis and disease. *Open Biol* 11(2):200360
- Nasser S, Bilston LE, Phan-Thien N (2002) Viscoelastic properties of pig kidney in shear, experimental results and modelling. *Rheologica Acta* 41(1–2):180–192
- Olsen L, Sherratt JA, Maini PK (1995) A mechanochemical model for adult dermal wound contraction and the permanence of the contracted tissue displacement profile. *J Theor Biol* 177(2):113–128
- Oster GF, Murray JD, Harris AK (1983) Mechanical aspects of mesenchymal morphogenesis. *Development* 78(1):83–125
- Park J, Kim DS, Shim TS, Lim CM, Koh Y, Lee SD, Kim WS, Kim WD, Lee JS, Song KS (2001) Lung cancer in patients with idiopathic pulmonary fibrosis. *Eur Respirat J* 17(6):1216–1219
- Perelson AS, Maini PK, Murray JD, Hyman JM, Oster GF (1986) Nonlinear pattern selection in a mechanical model for morphogenesis. *J Math Biol* 24(5):525–541
- Petrolli V, Le Goff M, Tadrous M, Martens K, Allier C, Mandula O, Hervé L, Henkes S, Sknepnek R, Boudou T et al (2019) Confinement-induced transition between wavelike collective cell migration modes. *Phys Rev Lett* 122(16):168101
- Scianna M, Bell CG, Preziosi L (2013) A review of mathematical models for the formation of vascular networks. *J Theor Biol* 333:174–209
- Serra-Picamal X, Conte V, Vincent R, Anon E, Tambe DT, Bazellieres E, Butler JP, Fredberg JJ, Trepast X (2012) Mechanical waves during tissue expansion. *Nat Phys* 8(8):628–634
- Snedeker JG, Niederer P, Schmidlin F, Farshad M, Demetropoulos C, Lee J, Yang K (2005) Strain-rate dependent material properties of the porcine and human kidney capsule. *J Biomech* 38(5):1011–1021
- Thompson DW (1917) *On growth and form*. Cambridge University Press, Cambridge
- Tlili S, Gauquelin E, Li B, Cardoso O, Ladoux B, Delanoë-Ayari H, Graner F (2018) Collective cell migration without proliferation: density determines cell velocity and wave velocity. *R Soc Open Sci* 5(5):172421
- Tosin A, Ambrosi D, Preziosi L (2006) Mechanics and chemotaxis in the morphogenesis of vascular networks. *Bull Math Biol* 68(7):1819–1836

- Tranqui L, Tracqui P (2000) Mechanical signalling and angiogenesis. the integration of cell–extracellular matrix couplings. *Comptes Rendus de l'Académie des Sciences-Series III-Sciences de la Vie* 323 (1), 31–47
- Tranquillo RT, Murray JD (1992) Continuum model of fibroblast-driven wound contraction: inflammation-mediation. *J Theor Biol* 158(2):135–172
- Turing AM (1952) The chemical basis of morphogenesis. *Philos Trans R Soc London B* 237:37–72
- Urdu S (2012) On the evolution of morphogenetic models: mechano-chemical interactions and an integrated view of cell differentiation, growth, pattern formation and morphogenesis. *Biol Rev* 87(4):786–803
- Valtorta D, Mazza E (2005) Dynamic measurement of soft tissue viscoelastic properties with a torsional resonator device. *Med Image Anal* 9(5):481–490
- Van Helvert S, Storm C, Friedl P (2018) Mechanoreciprocity in cell migration. *Nat Cell Biol* 20(1):8–20
- Verdier C (2003) Rheological properties of living materials from cells to tissues. *Comput Math Methods Med* 5(2):67–91

Publisher's Note Springer Nature remains neutral with regard to jurisdictional claims in published maps and institutional affiliations.